Long-Wave Infrared Frequency Combs Based on Quantum Cascade Lasers

by

Tianyi Zeng

B.S., Tsinghua University (2014)

Submitted to the Department of Electrical Engineering and Computer Science
in partial fulfillment of the requirements for the degree of

Master of Science in Electrical engineering and Computer Science

at the

MASSACHUSETTS INSTITUTE OF TECHNOLOGY

Septermber 2017

Author .....
Department of Electrical Engineering and Computer Science
August 31, 2017

Certified by .....
Qing Hu
Professor of Electrical Engineering and Computer Science
Thesis Supervisor

Accepted by .....
Leslie A. Kolodziejski
Professor of Electrical Engineering and Computer Science
Chair, Department Committee on Graduate Students

Long-Wave Infrared Frequency Combs Based on Quantum Cascade Lasers

by

Tianyi Zeng

Submitted to the Department of Electrical Engineering and Computer Science
on August 31, 2017, in partial fulfillment of the
requirements for the degree of
Master of Science in Electrical engineering and Computer Science

Abstract

Ever since the invention of quantum cascade laser (QCL), the performance and the flexibility in design has made it a desirable source for a wide range of applications, such as trace-chemical sensing, health monitoring, frequency metrology, noninvasive imgaing and infrared countermeasures. The LWIR region (or mid-infrared region), roughly ranging from 2-20 μm, is of particular importance to spectroscopy applications, since many molecular species have their strongest rotational-vibrational absorption bands in that area. Infrared laser spectroscopy began about 40 years ago and has been using a variety of different tunable laser-based sources, particularly lead salt diodes, color center lasers, difference frequency generation and optical parametric oscillators. The large tunabilitiy in the design (lasing frequency, tunability, power, material system, etc.) and the compactness in fabrication and packaging has made QCL an ideal source for laser-based spectroscopy. Traditional spectroscopy systems suffer from problems like large physical dimensions, long data-processing times and spectral resolution restrictions. Therefore the development of a simple, robust, compact and inexpensive optical source/system like QCL frequency combs can largely benefit spectroscopy systems. In the past few years, QCLs have proven to be able to form comb radiation in both LWIR and THz regions. And dual comb spectroscopy has been demonstrated using QCL frequency combs with very short acquisition time (μs). The development of a broadband, high power, narrow linewidth and stable LWIR frequency comb based on quantum cascade laser is the key to realizing such broadband ultrafast spectrometer in the mid-infrared range.

This thesis explores the design, fabrication and characterization techniques towards the development of LWIR QCL frequency comb devices for spectroscopic purposes. A complete wet etch epi-up fabrication process is reported, with preliminary results on the dry-etch technique to incorporate dispersion compensation strucutre and epi-down fabricaiton for high power CW mode QCL device. Formation of comb(-like) regime has been observed in two devices, with the Gires-Tournois Interferometer (GTI) mirror providing dispersion from the rear facet. In order to improve the comb performance of these devices, dispersion of the device is measured to provide essen-

tial information for the design of chirped top cladding for dispersion compensation. This thesis provides an important step towards the realization of a room temprature, broadband, CW mode LWIR QCL frequency comb device for spectroscopic purposes.

Thesis Supervisor: Qing Hu
Title: Professor of Electrical Engineering and Computer Science

Acknowledgments

First and foremost, I would like to thank my research advisor, Professor Qing Hu, for giving me the chance to take on this waterfall-like adventure along the cascaded quantum structure. The support and guidance he provided has made my last two years very exciting and fulfilling. I'd also like to thank Dr. David Patrick Burghoff, for setting a good example of a dedicated, resourceful and rigorous researcher, and also for the experimental and theoretical skills he has taught me. I would also like to acknowledge all the other current group members, Yang Yang, Ali Khalatapour, Andrew Keith Paulsen, Yuri Victorovich Flores and Asaf Albo, for all the enlightening discussions and the support they showed when I am lost. My gratitude also goes to all the former group members, whose work has built the very foundation of our current research.

I thank our long-term collaborator Dr. John L. Reno from Sandia National Laboratories, for the MBE grown wafers he has been working so hard to provide for this work. I would also like to thank all the other team members on the DARPA project that makes this work possible, they are: Prof. Gerard Wysocki's group from Princeton University and Prof. Jacob Khurgin's group from Johns Hopkins University. Special thanks also goes to Dr. Mykhaylo P. Semtsiv and Prof. W. Ted Masselink from Humboldt University of Berlin for the high quality MBE growth they have provided. I would also like to thank four other research groups from around the globe for providing either MBE grown wafers or fully packaged devices: Prof. Markus Amann's group from Walter Schottky Institute in Technical University of Munich, Dr. Gottfried Strasser's group from TU Wien, Prof. Qijie Wang's group from Nanyang Technological University, and Dr. Masamichi Yamanishi's group from Hamamatsu Photonics. Lastly, I would like to thank Dance Revelasian, MIT ADT, MIT Syncopasian for giving me the best group of friends and most awesome performing experiences, and my mother, father, cousin and grandparents for offering me the most love a person could ever wish for.

Contents

List of Figures

List of Tables

Chapter 1

Introduction

Quantum Cascade Lasers (QCL), as compared to conventional semiconductor lasers, operates on a different mechanism, where photons are generated by consecutive inter-subband transitions. Those transitions occur between confined electron states formed by quantum wells, which was only enalbed by the advancement in epitaxy technology. Since only one type of carriers, electrons, is required, it is a type of unipolar semiconductor laser. Since the invention of QCL in 1994 by J. Faist, F. Capasso and coworkers [25], the technology has advanced rapidly due to its intrinsic design flexibility enabled by quantum engineering.

In this chapter, the history of development for QCL devices is summarized in three wavelength regions, namely, short wavelength infrared (3-5 μm), long wavelength infrared (LWIR) (5-15 μm) and THz (30-300 μm).

1.1 Brief History of QCL Development

One cannot simply build a great wall out of bare hands, just like how one cannot even imagine a device as complicated as QCL with the fabrication techniques available before 1950s, befoe the invention of Molecular Beam Epitaxy (MBE).

Many people regard Feynman's well-known lecture [26] in December 1959 as the beginning of nanotechnology. From a historian's point of view, as W. Patrick McCray points out in his article [27], Feynman's lecture was much less influential than we

thought. And the roles of the advancement in experimental techniques have been much overlooked, with MBE being one of the most important ones. MBE is the technique to grow crystalline thin films in ultrahigh vacuum (UHV) with precise control of thickness (down to the atomic level), composition and morphology.

On one hand, it provides unique opportunity for researchers to study crystal growth on a subnanometer scale. On the other hand, MBE enables the growth of artifically designed crystals with high precision and reproducibility. The invention and development of MBE was largely credited to J. R. Arthur [28] and A. Y. Cho [29] for their work on GaAs epitaxial growth in the late 1960s. But as Arthur mentioned in his paper, Gunther's work [30] solved the technical difficulty of excess gas flux during growth, and laid the foundation for the sucess demonstration of MBE.

After the development in MBE technology, researchers started their exploration with this technology. In 1970 Esaki and Tsu's demonstrated a one-dimensional superlattice with periodic variation of impurity density introduced druing epitaxial growth [31] . Then the idea of QCL was proposed by Kazarinov and Suris in 1971 [32]. And after more than twenty years of development, the first QCL was demonstrated in 1994 at Bell labortaries by J. Faist et al. [25].

The development of QCL has rather accelerated ever since. Single mode device at room temperature was demonstrated in 1997 [33], lasing at both 5.4 μm and 8 μm. Five years later, continuous wave operation of mid-infrared QCL at room temperature was reported [34].

Ever since its introduction, QCL have been designed and fabricated in a wide emission range, from $\sim$3 μm to several hundreds of μm. Different literatures categorize QCL in terms of the emission wavelength in different ways [35], in the context of this thesis, the author would like to divide QCL devices into 3 different wavelength regions: short wavelength (3 μm – 5 μm), LWIR (5 μm – 15 μm), and THz (30 μm – 300 μm), or more frequently written in terms of frequency 1 THz – 10 THz). Although the underlying mechanisms for QCLs are the same, devices in different spectral regions usually use different material systems, and hence have different fabrication process, challenges, characteristics and performance. As mentioned before,

this thesis will mainly focus on the IR QCL development, but in this chapter, the theory and fabrication for the other two types of devices will also be introduced.

Before we delve into the discussion of QCL development in each wavelength region, explanation to the choice of the terms is needed. To start with, infrared radiation (IR) is usually defined as electromagnetic radiation with wavelength ranging from 700 nm to 1 mm [36]. Different sources do have slightly varying ranges, some starts at 750 nm [37], some at 800 nm [38]. But that doesn't affect our discussion, since the QCL emission wavelength range is very far away from the red edge of visible spectrum. A commonly used sub-division scheme [24] is listed in Table 1.1. The IR-A, IR-B and IR-C division scheme was recommended by Internationl Commission on Illumination (CIE). And the IR-C covers both Mid-wavelength and Long-wavelength infrared.

As we can see in the table, there are some overlap as well as discrepancies between the notation used in this thesis and the ones mentioned above. It is due to the fact that the bottom of QCL emission range is ~ 3 μm while IR starts at 750 nm. QCL community calls the shortest lasing QCLs short-wavelength devices [39], which are typically built on strain-balanced material systems or non InGaAs/InAlAs-InP systems. And the ones with longer emission ranges are mentioned either as mid-wavelength (MidIR, mid-infrared) or long-wavelength (LWIR) devices. In the context of this thesis, the author would like to adopt the convention from the QCL community. LWIR and MidIR would both be used to refer to devices lasing at 5 μm – 15 μm.

Division Name	Abbreviation	Wavelength	Frequency
Near-infrared	NIR, IR-A	0.75 – 1.4 μm	214 – 400 THz
Short-wavelength infrared	SWIR, IR-B	1.4 – 3 μm	100 – 214 THz
Mid-wavelength infrared	MWIR, MidIR, IR-C	3 – 8 μm	37 – 100 THz
Long-wavelength infrared	LWIR, IR-C	8 – 15 μm	20 – 37 THz
Far-infrared	FIR	15 – 1000 μm	0.3 – 20 THz

Table 1.1: IR subdivision scheme [24]

1.1.1 Short-wavelength QCL Development

QCLs operating in short wavelength region(3 - 5 μm) fit into the midinfrared atmospheric window, and are driven by various applications including environmental and medical gas sensing, communication and military uses. The first short-wavelength QCL emitting in this range at 3.5 μm was demonstarted by Faist et al. in 1998 based on strain compensated InGaAs/InAlAs-InP[1] material system [39]. For this first demonstration, pulsed mode operation up to 280 K was reported, while CW operation achieved 120 mW in power at 15 K. In 2000, room temperature QCL in this range was reported by F. Liu et al. from China [40]. The same material system (InGaAs/InAlAs-InP) was used, and lasing at 3.54 - 3.7 μm was observed at room temperature. Four years later, room temperature short-wavelength QCL was reported using two other material systems: strain-compensated InGaAs/AlAs-InP, lasing between 3.7 - 4.2 μm [41]; InAs/AlSb-InAs, lasing at $\sim$4.5 μm [42]. In the same year, a novel approach was demonstrated by Gmachl et al. [43], where second harmonic generation (SHG) at 3.5 μm was produced by a DFB QCL at 7 μm.

The first room temperature continuous wave operation of QCL in this range was first demonstrated by Yu et al. from Razeghi's group [44] in 2005 on strain-balanced InGaAs/InAlAs-InP material system, with a power of 166 mW at 298 K. In 2006, multiple groups reported QCL lasing in this region [45, 46, 47, 48]. Q. Yang et al. demonstrated room temperature short wavelength QCL lasing at $\sim$3.7 μm using InGaAs/AlAsSb-InP material system [45]. Devenson et al. reported lasing at very small wavelength $\sim$3 μm using the very high conduction band offset of the InAs/AlSb-InAs material system [46]. Before Devonson's 2006 paper, the major constraint for a shorter wavelength QCL emission was the lack of an efficient low-loss waveguide. In their paper, they utilized plasmon enhanced waveguide design made of heavily doped n-InAs cladding layers and InAs/AlSb superlattice spacers, which was first proposed by Sirtori et al. in 1999 [49]. Room temperature continuous wave operation at 4 μm was demonstrated by Yu et al. [48], with a doulbe-phonon resonant active region to

[1]The convention A/B-C means the device has MBE grown structure made of materials A and B grown on substrate C. This convention will be used over the context of this thesis

reach higher emission energy as compared to their work in 2005.

In the past 10 years, researchers have been pushing forward the performance of short-wavelength QCLs in terms of higher operating temperature, higher power and wall plug efficiency, tunability etc. In 2007, Devenson et al. reported 300 K lasing at 3.3 μm, [50]. One year later, 1.3 W power was reached at room temperature in CW operation by Bai et al. [51].

In 2013, O. Cathabard and A. Baranov et al. demostrated QCL near 2.6 μm on InAsr/AlSb-InP material system [52]. Three years later, T. Kreczek et al. achieved 85 nm of tuning around 3.2 μm with external cavity [53].

1.1.2 LWIR QCL Development

In earlier days of QCL history, devices based on InGaAs/InAlAs-InP system have shown a wide emission range covering the two atmospheric windows (3.4 μm – 13 μm, [39, 54, 55]), making them promising candidates for communication applications. The short-wavelength QCLs discussed above, covers the first atmospheric window ($\sim$ 4.5 μm – 5.5 μm), while the topic of this section, the LWIR QCLs covers the second one ($\sim$ 7.5 μm – 14 μm).

The first demonstration of QCL used the same material group (lattice matched InAlAs/InGaAs-InP) as the majority of LWIR QCLs [25], although it lased at 4.2 μm, not quite in the LWIR range defined in this thesis, we would still categorize it as the very first demonstration of LWIR QCLs. A peak power of 8 mW was observed at 10 K in pulse mode. The effort of the community was then focused on widening the spectrum coverage, pushing for higher temperature in pulsed mode, and eventually room temperature CW operation.

Pulsed mode operation above room temperature of LWIR QCLs have been reported shortly afterwards (5 μm [56], 8.5 μm [54]). Devices with wavelengths as long as 11 um has also been demonstrated in 1996 [57]. Single mode distributed feedback laser (DFB) above room temperature (pulse mode) was demonstrated in 1997 [33], lasing at both 5.4 μm and 8 μm. This device has a tuning range of 7.78 μm - 7.93 μm with temperature between 80-315 K. Continuous wave operation above room temper-

ature of mid-infrared QCL was not demonstrated untill 2002 [34]. The device was reported to lase at 9.1 μm up to 312 K in CW mode. Besides from the double-phonon resonance design in the gain medium, several other technical details also contribute largely to its sucess: buried heterostructure waveguide design, high-reflection coating on both facets, and epi-down mounting techniques (or junction-down mounting as mentioned in the paper).

Other than CW room temperature operation, a broadly tunable spectral range is also desired for LWIR QCLs for spectroscopy purposes. Grating-tuned external-cavity QCL was reported in 2001 [58], with a tuning range of $\sim$23 nm at 203 K in pulsed mode. That requires a high gain broadband active region covering the desired tuning range. It can be achieved by cascading different gain media designs in one active region [59]. The so-called heterogenenous QCLs was then used in EC-QCLs to improve the tuning range and output power [60, 61]. In 2009, broadband tuning of a five cascade EC-QCL was reported with a tuning range 7.6-11.4 μm ($\sim$432 cm^{-1}) [62].

Another important aspect for QCL performance is power and power efficiency. The metric widely used to characterize efficiency is wall plug efficiency (WPE), which is essentially the conversion efficiency between electrical power and optical power. High power QCL device is important to numerous applications including photoacoustic spectroscopy, remote sensing, infrared countermeasures and free space communications [63]. Power efficiency becomes important only when power consumption, heat dissipation and device size is of concern to application purposes, for instance, trace chemical sensing, health monitoring and compact mid-IR spectroscopy [18, 64].

The first QCL had a peak power of 8 mW and WPE of lower than 0.15% in pulsed operation at 10 K [25]. Over the years, both power and WPE have experienced huge improvement. A steady improvement for WPE was kept from 7% pulsed and 3.7% cw in 2004 [65], to 27% pulsed and 21% cw in 2011 [66]. As for power, watt-level power ouput in room temperature cw operation can already be routinely produced [67, 68], with single facet room temperature cw power as high as 5.1 W [66].

Other than InGaAs/InAlAs-InP, different material system has also been reported

to demonstrate QCL in this region. In 2009, M. Nobile and G. Strasser utilized Al-free material system InGaAs/GaAsSb-InP, achieved lasting at 11.3 μm at 78K [69].

Noticeably, ever since the first demonstration of QCL based mid-infrared frequency comb [6], mid-infrared QCL has become a very promising candidate as the source for a compact, all solid-state mid-infrared spectrometer. The discussion on QCL based mid-infrared frequency combs will be covered in the next chapter.

1.1.3 THz QCL Development

THz range of the electromagnetic spectrum (ν ~1–10 THz, λ ~30–300 μm) has long been of interest to research institutes as well as industries for the numerous potential applications it enables, including but not limited to astronomy, atmospheric science, hazardous material detection, non-invasive biological and medical imaging [70], tomography [71], wireless communication [72] and ultrafast spectroscopy. Despite numerous applications and great desire for a compact and coherent THz radiation source, the THz frequency range remained relatively undeveloped mainly for the following two reasons: (a) Lack of appropriate materials with sufficiently small bandgaps for direct generation of THz radiation; (b) Lack of proper mode confinement and waveguiding strategy for the relative large wavelength (10x times that of LWIR region).

Different approaches have been reported to generate THz radiation (Fig. 1.1), such as QCL, uni-travelling-carrier photodiode (UTC-PD), difference frequency generation (DFG), ultrafast photocurrent in photoconductive switch (as seen in THz-TDS [73]), resonant tunnelling diodes (RTDs) etc., which are well summarized in this review [1].

THz QCL, as compared to other candidates, has the advantage of being compact, mass-producable and widely tunable. The absence of longitudinal-optical (LO) phonon emission at low temperature (because photon energy is smaller than LO phonon energy at THz frequency range, E_{LO}=36 meV in GaAs, equivalent to 8.7 THz), suppresses the transition from upper subband to lower radiative states, which counters the formation of population inversion. Because of that, although the first observation of intersubband emission took place in THz [74], the first demonstration

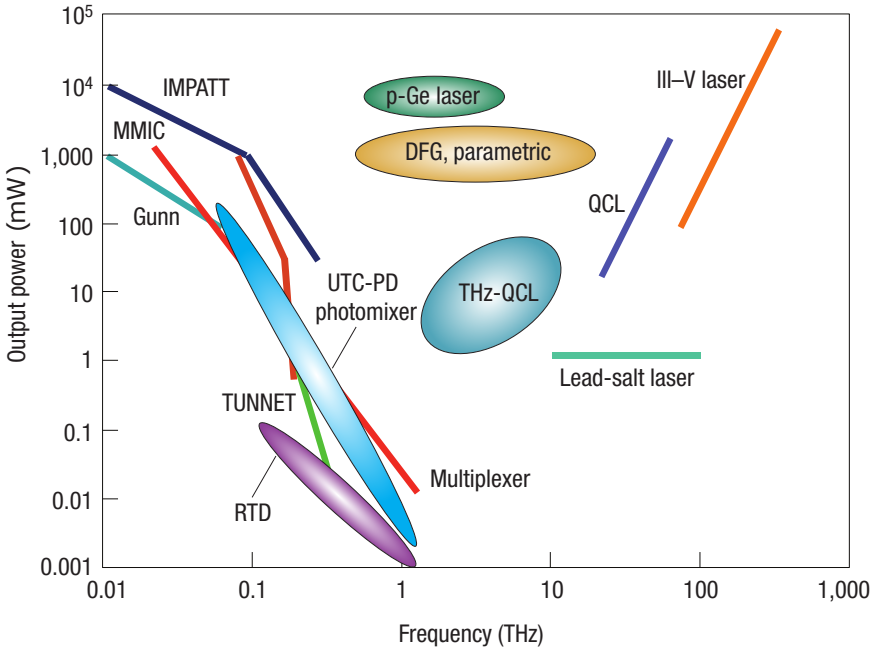

Figure 1.1: Different THz emission approaches (power vs. frequency) [1].

of THz QCL [75] took place many years after their mid-infrared counterpart. In 2002, the first THz QCL was reported lasing at 4.4 THz with output power of >2 mW at 50 K, using GaAs/AlGaAs-GaAs material system.

There are two specific gain media designs that the author would like to briefly introduce, that conquered the population inversion in the early days of THz QCL development. First is the bound-to-continuum design reported by Faist's group (3.5 THz) [76], where extraction occurs through a diagonal transition to miniband to reduce minimize lower state population. This design is essentially a scaled version of a bountd-to-continuum gain medium for mid-infrared QCL [77]. The second one is the resonant phonon design (LO phonon depopulation) by Hu's group (3.44 THz) [78], which resonantly injects electron into the upper state and entice the extraction of lower state electrons through LO phonon scattering. This design has many variations and produced the devices with the highest pulsed mode operating temperature: 186 K in 2009 [79], 200 K in 2012 [80].

Over the years, the spectral coverage, maximum operating temperature and power of THz QCL has improved significantly. Lasing frequency as low as 1.59 THz [81] has been achieved on a resonant phonon one-well injector design, and 1.39 THz with

magnetic field applied [82]. As mentioned before, pulsed mode operation has a highest operating temperature of 200 K [80], with continuous wave mode at 117 K [83]. In terms of power, 248 mW peak power in pulsed mode and 138 mW in CW was reported by Qing's group in 2006 [84]. Watt level pulsed peak power (1.01 W) was first realized by Linfield's group in 2014 [85], and only recently in 2017, 2.4 W output power at 4.4 THz was reported by the same group [86].

Notably, room temperature CW mode operation of THz source through DFG of dual-wavelength mid-infrared QCLs was reported [87], though peak power suffered (0.12 mW pulse).

The recent demonstration of THz frequency combs [5, 88, 8] has proven THz QCL to be the ideal source for compact, broad-band spectrometer. Along with the earlier report of mid-infrared frequency comb based on QCL [6], they together led the explosion of QCL-based spectrology research and development.

1.2 Thesis Overview

This thesis describes the fabrication techniques and preliminary characterization results of LWIR QCLs towards the development of frequency comb devices desirable for spectroscopy purposes. Chapter 2 discusses the basic theory, technology and applications of QCL ferquency combs. Chapter 3 introuces LWIR QCL techniques which are imortant in the design and fabrication of these devices. Chapter 4 covers the details of different fabrication processes developed and optimized for this work, with images of processed samples. Finally, chapter 5 presents characterization results on 3 different devices fabricated with the optimized fabrication process, including basic electrical, optical and spectral haracterization, beatnote measurement and dispersion measurement.

Chapter 2

LWIR Quantum Cascade Laser Frequency Combs

The mid-infrared spectral region of 2-20 μm (500-5000 cm^{-1}) [1] is of huge interest to researchers in many areas, due to the strong rotational-vibrational absorption bands experienced by many molecules in that wavelength. The strong transition makes mid-infrared spectroscopy a univocal way to identify and quantify molecular species. And this frequency range covers two of the atmospheric windows where the Earth's atmosphere is relatively transparent. This makes mid-infrared spectroscopy very attractive to environmental, security and industrial applications. Fourier transform infrared spectroscopy (FTIR) is the established technique to conduct mid-infrared spectroscopy. However, large physical dimensions, mechanical instability caused by moving structures and long data-acquisition and processing time has largely limited its use in laboratories with complete setups. Although recent advances in industries has allowed the development of portable FTIR systems [2], the fact that spectral resolution is inversely proportional to the length of the moving arm transforms the limit on physical size to the limit on resolution. For a handheld product with the size of ∼20 cm, the spectral resolution is only 4 cm^{-1}. Thus mid-infrared spectroscopy

[1] The spectral range used here is slightly different compared to the one we defined in Chapter 1 (similar to MidIR & LWIR combined). This is not uncommon among different research societies. The schemem here is adopted from [2].

[2] https://www.thermofisher.com/order/catalog/product/TRUDEFENDERFTX

technology and its applications can greatly benefit from a simple, robust, compact optical system. Frequency comb, the topic of this chapter, is the answer to those concerns and limitations.

2.1 Fundamentals of Frequency Comb

Frequency comb is a group of evenly spaced sharp peaks in the frequency domain (Fig. 2.1). It is traditionally generated by a pulse train of femtosecond mode-locked lasers [89]. The modulation frequency (frequency spacing between each comb lines) is the pulse repetition rate $v_g/2L$, which is the inverse round-trip time within the cavity of length L at a group velocity of v_g. Also because the frequency of each mode is determined by its phase velocity, which is different from v_g in most cases, the mode frequencies are then expected to deviate from being exact harmonics of pulse repetition rate f_{rep}. Therefore a constant phase difference $\Delta\phi$ exists between the electric field (carrier) and the envelope of each pulse (as shown in Fig. 2.1). This phase shift gives rise to the non zero offset frequency in the frequency domain, which is usually called carrier-envelope offset frequency (f_{ceo}). The fourier transform of the electic field will be a discrete set of equidistant, sharp frequency components f_n that follows: $f_n = nf_{rep} + f_{ceo}$, where $f_{ceo} = \Delta\phi f_{rep}/2\pi$.

2.2 Different Comb Formation Mechanisms

Laser frequency comb was introduced in the late 1990s [89, 90] as a tool for precise optical frequency metrology. Femto-second mode-locked lasers will generate equidistant comb lines in the frequency domain. Before that, optical frequency interval dividers (Fig. 2.2) [3] and harmonic frequency chains [91] were used to realize optica-to-radio frequency conversion for precise frequency measurement. For both measures, large numbers of stages is required to reach detectable radio frequency, it makes the set up highly complex, large and delicate. Not to meantion that each set up is only built for one single optical frequency. The introduction of femtosecond mode-locked laser

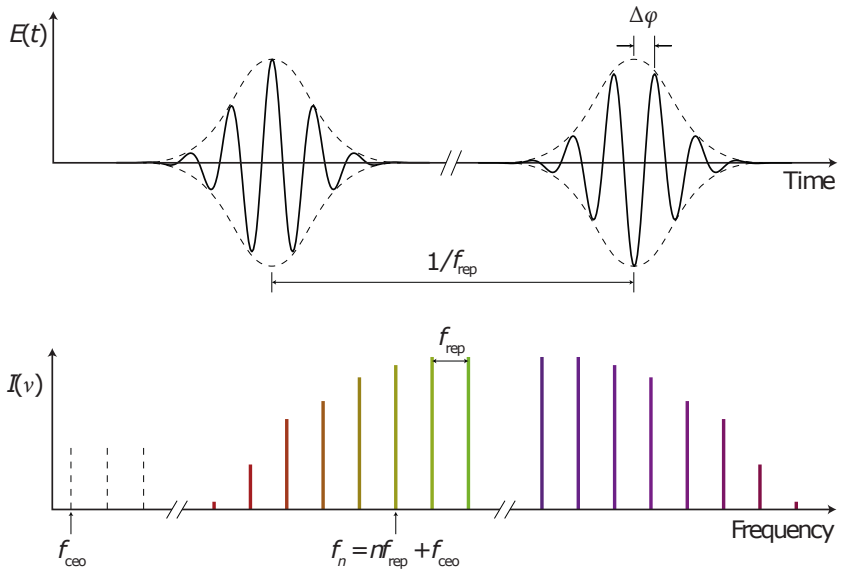

Figure 2.1: Time domain representation of a frequency comb pulse train together with the frequency domain comb lines. [2]

frequency combs provides an all solid-state, compact and robust alternative.

There are a number of other techniques that has been demonstrated to produce mid-infrared frequency combs, including difference-frequency generation (DFG) using nonlinear optical effects to transfer near-infrared frequency comb to the mid-infrared range [92], optical parametric oscillation (OPO) pumped by a signal comb with $\chi^{(2)}$ medium providing the gain, and microresonator based combs (Fig. 2.3) [93]. When pumped with a CW laser, the third-order nonlinearity $\chi^{(3)}$ of the dielectric resonator will lead to four wave mixing (FWM) and generate the comb (more details of four wave mixing will be covered in the next section).

As shown in Fig. 2.3, microresonator frequency combs have been demonstrated on different material systems and geometries. SiN ring resonator, with a fully planar structure, has the unique advantage of being CMOS-compatible, and is also equipped with dispersion engineering schemes [94] through atomic layer deposition (ALD) of HfO2 (also a standard CMOS material). Moreover, the recent demonstration of a pumping scheme for comb generation without external laser source [95] has offered great potential for this platform to be an on-chip broadband multiple wavelength source. Given all these advantages, however, this platform has a Q factor several

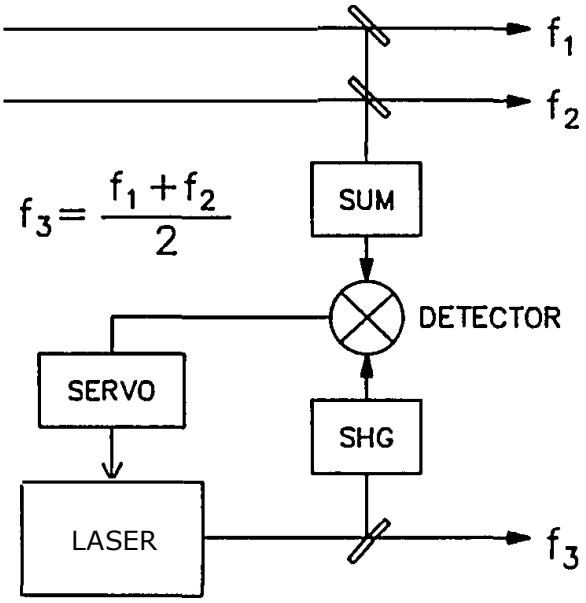

Figure 2.2: An optical frequency interval divider sums two input laser frequencies, f_1 and f_2. The third laser frequency f_3 can then be determined precisely relative to the mid point $(f_1 + f_2)/2$ by the detectin the beat note between the doubled third frequency $2f_3$ and the sum frequency. [3]. If n stages of divider are used in series, the frequency gap can be divided by a factor of 2^n untill it is accessible to radio frequency.

orders of magnitude lower than those of silica or crystalline resonators. That is partially compensated by the higher third-order nonlinearity of SiN.

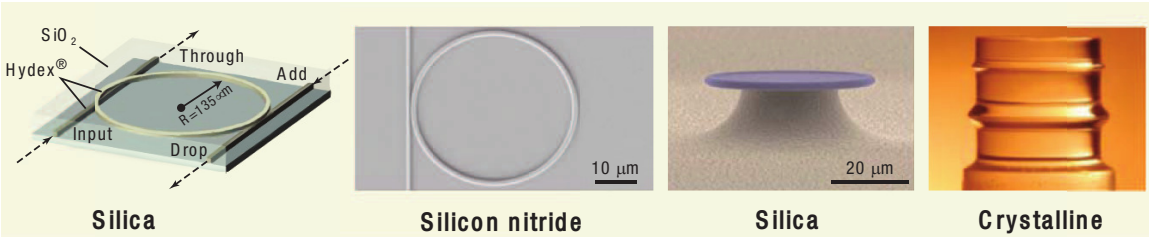

Figure 2.3: Experimental microresonator frequency comb systems. From left to right: Silica waveguides on a chip; silicon nitride (SiN) ring resonators; ultrahigh Q toroidal microresonator on a silicon chip; and ultrahigh Q milimeter-scale crystalline resonators. [4]

2.3 Frequency Comb Based on Quantum Cascade Laser

Demonstrations of frequency comb generation based on quantum cascade lasers in both mid-infrared [6] and THz [5] range has provided a novel comb source using direct electrical injection. Unlike its predecessors, no complex chain of optical components are required. Coolers, however, are needed for CW operation of the QCL comb device, but for the operatoin temperature of -20 $^{\circ}C$ for mid-infrared range, chipsized thermoelectric cooler can handle the job easily. For THz comb devices, the operating temperature of 40 K is indeed out of reach for portable-size cooling devices, but with the development of new gain media and the assist of the computational enhanced method that can largely simplify any coherent multiheterodyne spectroscopy system [96], the operation of THz combs at higher temperatures are within reach. Unlike THz QCL comb devices, mid-infrared QCL has a much shorter upper state lifetime $\tau \sim 0.3\ ps$ than the cavity round trip time ($\sim 50 - 100\ ps$ in a few mm cavity). This makes it difficult to achieve mode-locking for mid-infrared QCls. Essentially, in contrast to saturable absorbers used for mode-locking, the mid-infrared gain medium serves as a *reverse saturable absorber* or a *saturable gain* [97], which favors CW radiation. Each time the pulse travels in the cavity with a saturable absorber it gets shorter, while in a mid-infrared QCL, it gets broader. This reveals the frequency-modulated nature (as compared to amplitude-modulated signal from femtosecond pulses) of the mid-infrared QCL frequency comb device, which is further confirmed by the autocorrelation of the intermode beat data [6].

Unlike mode-locked lasers, this CW comb does not produce equal phase for all modes, instead, a stable relationship between all modes are achieved over the whole spectrum. A low GVD is essential to obtain such a stable phase relationship, for mid-infrared comb device, it is achieved through operating at the zero-GVD point of a broadband heterogeneous gain medium. While for the THz counterpart, because the dispersion is so high at this frequency, dispersion compensaton has to be implemented through chirped corrugation (Fig. 2.4) [5]. And due to the frequency-modulated

nature of the comb, there will be no high intensity peaks during operation, which helps avoid deleterious nonlinear efects, optical damage and detector saturation. Beyond all that, a frequency-modulated signal is less susceptible to noise than an amplitude-modulated one.

Similar to microresonator based frequency combs, in QCL comb devices, the frequency conversion is generated through four wave mixing process, which originates from the intensity-dependent refractive index (Kerr effect, third order nonlinearity $\chi^{(3)}$). Two counterpropagating waves in the cavity at frequency ω_1 and ω_2 interacts though refractive index modulation and generates two new frequency components, the energy between modes are transferred at the beating frequency $\delta\omega = \omega_1 - \omega_2$:

$$\omega_3 = \omega_1 + \delta\omega = 2\omega_1 - \omega_2 \tag{2.1}$$

$$\omega_4 = \omega_2 - \delta\omega = 2\omega_2 - \omega_1 \tag{2.2}$$

When four different frequencies component interacting through this process, it is called non-degenerate four wave mixing. When two of the four frequencies coincide, it is the case of degenerate four wave mixing:

$$2\omega_1 = \omega_2 + \omega_3 \tag{2.3}$$

As shown in Fig. 2.4, in a QCL comb device, both degenerate and non-degenerate process are present, resulting in the proliferatoin of modes.

2.4 Frequency Comb Based Spectroscopy

The simplest way to exploit the full potential of frequency combs, namely the frequency resolution, frequency accuracy, broad bandwidth and power, for spectroscopic purposes, is through dual comb spectroscopy (DCS). Ever since the first demonstration [98], a large number of proof-of-concept experiments has been reported [99]. Demonstrations of dual-comb spectroscopy based on QCL frequency combs have also

been reported [7, 8, 88]. The technique is based on two QCL comb devices with slightly different mode spacing (f_{rep1} and $f_{rep2} = f_{rep1} + \delta f$). One comb serves as the local oscillator (LO), and the other is used to interrogate the sample. Comb signal from two paths will be combined and the multi-heterodyne beat is measured by the detector (Fig. 2.5.a). Each sampling comb line with the absorption information will beat with a corresponding line in the LO $n\delta f$ away, generating an RF signal with the difference frequency. In this way, the sampling comb will form a one-to-one mapping to a down-converted RF beat signal (also a comb), as shown in Fig. 2.5.b. The resolution of the absorption spectra is then defined by the comb spacing of the sampling QCL comb device, a spacing of 7.25 GHz will give a resolution of 0.25 cm^{-1} [7]. Multimode Fabry Perot (FP) QCL sources with slightly different FP mode spacings can also be implemented in a similar scheme to conduct multiheterodyne spectroscopy [100, 101].

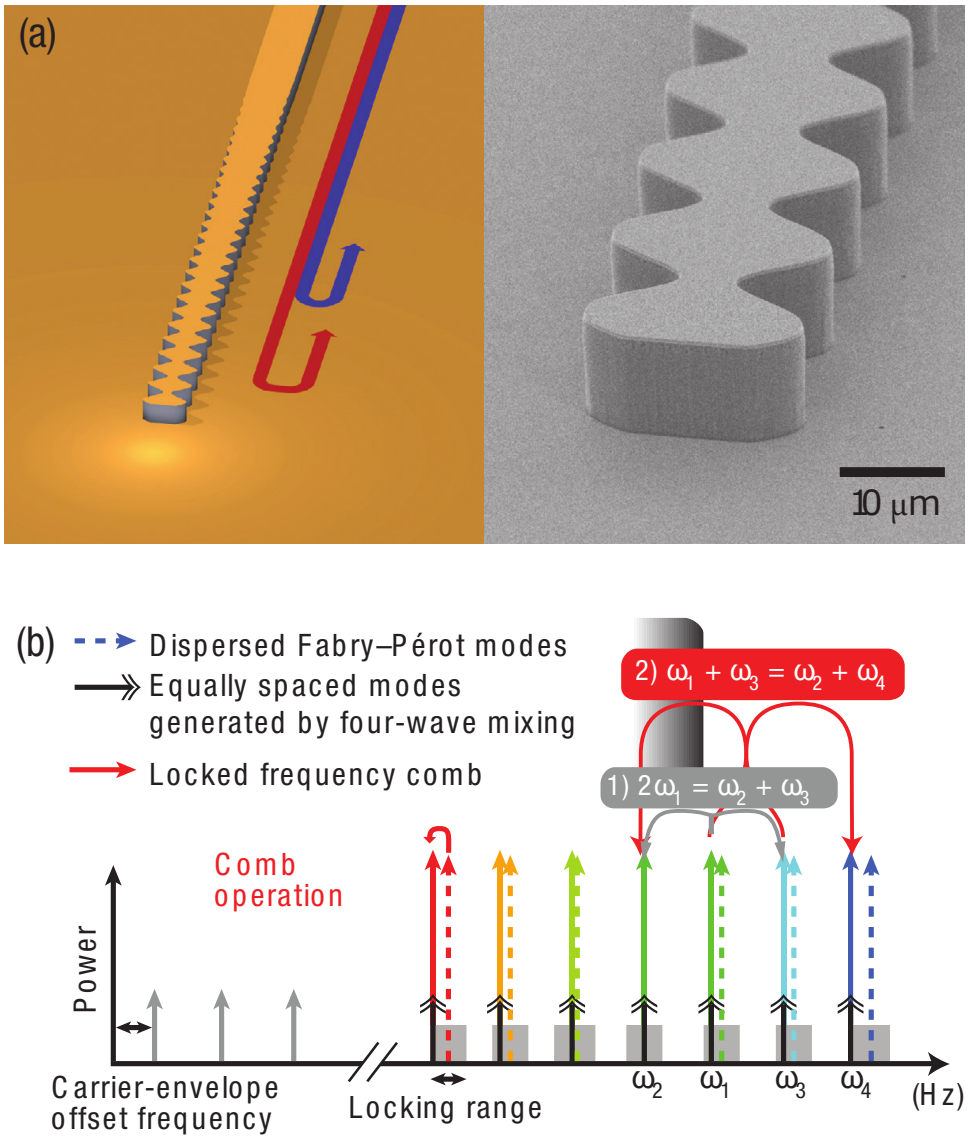

Figure 2.4: (a) Corrugation design for dispersion compensation in THz laser frequency comb device [5]. (b) Four-wave mixing processes in frequency comb [6].

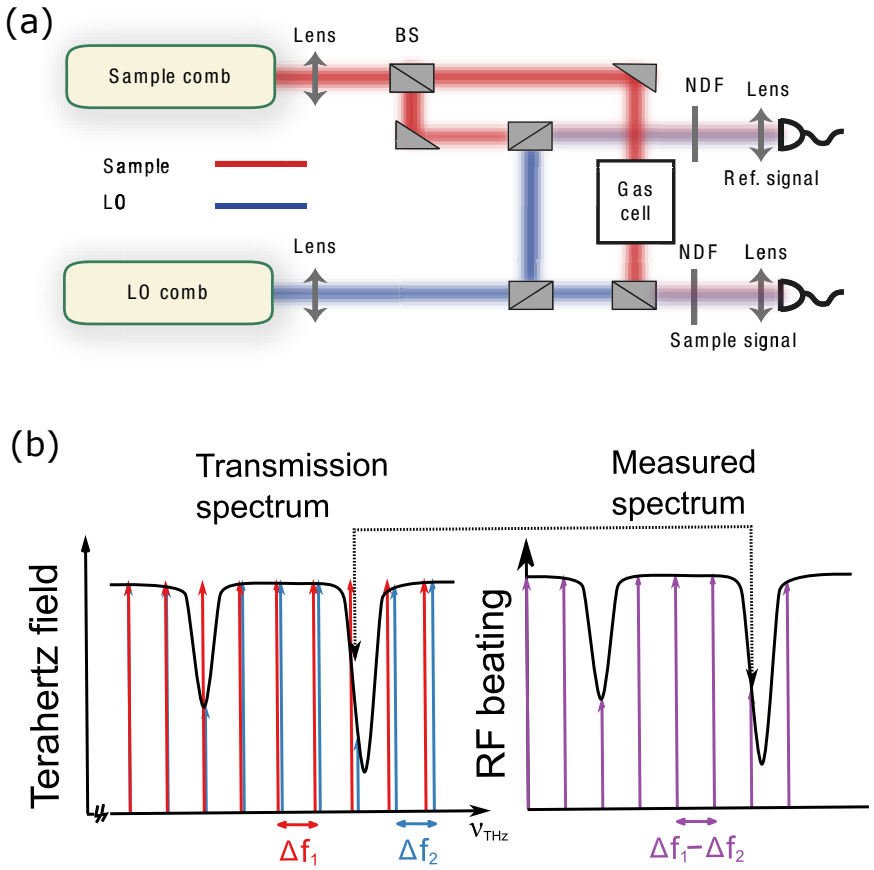

Figure 2.5: (a) Schematic of the dual-comb spectroscopy setup with QCL frequency combs. One comb is served as the local oscillator, the other is shined through the sample to obtain absorption information [7]. (b) One-to-one mapping between the lines in the optical frequency (with absorption information) and the lines in RF domain [8].

Chapter 3

LWIR QCL Techniques

In this chapter, key techniques crucial to the design and fabrication LWIR QCL devices are discussed. The author would like to cover as many topics as possible, but some quite important topics are not discussed here due to limit of space in the thesis and also because they are not directly related to the work presented here. Those topics include: QCL gain media design, material growth and characterization techniques and thermal modeling and management, anti- and high- reflection coating, etc. The understanding of those topics, along with the ones dicussed below, will establish a solid foundation for research in this field. For that reason, the author would like to introduce the following literatures (books, reviews and theses) which entail a more detailed discussion of all these topics [102, 54, 18, 103, 104, 13, 9, 105].

As introduced in the first chapter, in the LWIR range, lattice-matched InGaAs/InAlAs-InP ($In_{0.52}Al_{0.48}As/In_{0.53}Al_{0.47}As$) is the most commonly used material system for mid-IR QCLs [25, 33, 106, 67, 107]. It is also the material system used throughout the study in this thesis (except for the processed devices from Hamamatsu Photonics presented in Chapter 5, where strain compensated material system is used). The advangages of this combination includes: First, the electron masses (InGaAs: $m^* = 0.043m_0$) are relatively lighter, leading to smaller optical phonon scattering rates and larger oscillator strengths [104]; Second, the refractive index of InP (n = 3.1) substrate has a good contrast against InAlAs (n = 3.2) and InGaAs (n = 3.5), which is favorable for mode confinement in dielectric waveguides; Third, the relatively

large bandoffset (ΔE_c = 0.52 - 0.8 eV, Table 3.1) enables the design of QCL covering a large range of wavelengths [107].

	GaAs/AlGaAs	InGaAs/InAlAs	InGaAs/AlAsSb	InAs/AlSb
ΔE_c	0 - 0.035	0.5 - 0.8	1.6	2.1
m^*/m_0	0.067	0.043	0.043	0.023

Table 3.1: Band offsets (eV) and effective masses for various material systems.

3.1 Mode Confinement

3.1.1 Vertical Confinement

As shown in Fig. 3.1, we will structure the problem in the simplest dielectric slab waveguide model. The material (gain media) with refractive index n_1 is sandwiched between two semi-infinite cladding with lower refractive index (InP), satisfying $n_1 > (n_2, n_3)$. The model here is well-described in a lot of textbooks and will not be discueesd in full details here.

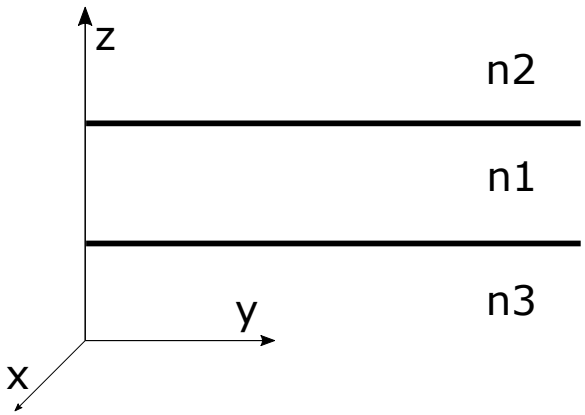

Figure 3.1: Schematic illustration of semi-infinite dielectric waveguide.

We consider the propagation of monochromatic radiation at frequency ω in y direction, assuming the material is homogeneous and source-free. Given the polarization selection rule of intersubband transitions, only TM mode (with E field in the growth direction) will be supported [108]. So we will only consider TM mode here.

The complex E field should satisfy Helmholtz equation (so does H), where n_i are the refractive indexes.

$$(\nabla^2 + {n_i}^2\omega^2/c^2) \times \mathbf{E} = 0 \tag{3.1}$$

The solution can then be constructed with plane waves propagating in the z-y plane, the phase factor in the y-direction is assumed to be common in all layers:

$$\mathbf{E} = \mathbf{E}_m e^{-ik_z z} e^{i(wt-\beta_m y)} \tag{3.2}$$

where β_m is the propagating constant of the mode with index m. From (3.1) we can derive the relation:

$$\beta^2 + {k_z}^2 = {n_i}^2\omega^2/c^2 \tag{3.3}$$

The value of β plays a very important role in the guiding condition. We define $k_0 = \omega/c$.

- if ($k_0 n_2$,$k_0 n_3$) $< \beta < k_0 n_1$, there will be guided mode, since k_z is real in the guiding layer and imaginary in the cladding layer.
- if $\beta >$ ($k_0 n_2$,$k_0 n_3$), leaky modes exist.

For the TM mode (where $E_y = 0$), where magnetic field is oriented along the y direction (it is **very important** to notice that the TE TM mode used here is the very opposite of what EM theory normally use, where for a TM mode, no magnetic field should exist in the propagation direction, which gives H_y=0. This is a historical error, the QCL society has been adopting this convention, where the supported mode is the ***TM*** mode.), the continuity at the interface requires [1]:

$$TE : \mathbf{H}_x, \mathbf{E}_y \tag{3.4}$$

$$TM : \mathbf{E}_x, \mathbf{H}_y \tag{3.5}$$

[1] A complete tangential boundary continuity condition for TM mode would include H_x, H_y, E_x, E_y. But since $E_y = 0$, and from Maxwell equations, H_x depends on $\partial E_z/\partial y$, which goes to 0 if we assume the lateral mode profile stays the same during propagation. That's why only two components are left. The same goes with the boundary conditions for TE mode.

And from Maxwell's equation:

$$\nabla \times \mathbf{H} = i\omega\epsilon_0 {n_i}^2 \mathbf{E} \tag{3.6}$$

The boundary conditions then corresponds to:

$$TM : \mathbf{H}_y, \frac{1}{n^2}\frac{\partial \mathbf{H}_y}{\partial z} \tag{3.7}$$

Switch (3.7) the TM boundary conditions from H field to E field:

$${n_i}^2 \mathbf{E}_z, \frac{\partial \mathbf{E}_z}{\partial z} \tag{3.8}$$

Solving (3.8) at the interfaces of the waveguide will yield possible values of the propagation constant β_m. Apparently, it will be a function of d (the gain media thickness) and λ. When there is only one possible β value, we call it single mode waveguide, multimode otherwise.

We usually define the effective index as:

$$n_{eff} = \frac{\beta}{\omega/c} \tag{3.9}$$

For confined modes, its value should lie between the refractive index of the core and cladding. Knowing the thickness of the active region and the material and doping of all layers, we will be able to analytically calculate the mode profile in the growth direction. For InGaAs/InAlAs-InP system, the most basic vertical confinement structure along with the mode profile is shown in Fig. 3.2.

As mentioned before, the InP–active region (InGaAs/InALAs)–InP waveguide will provide good confinement in the vertical direction, due to the contrast in the refractive index. However, the confinement is never perfect, there will always be a part of the radiation leaking into the cladding area, depending on the absolute value of the imaginary k_z for the cladding area. This reduces the performance of the device, as only the core part can provide optical gain when biased. Thus the overlap factor

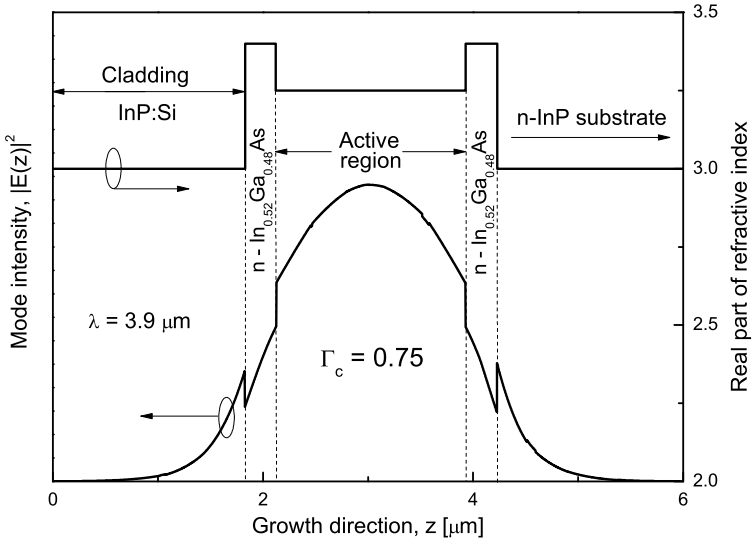

Figure 3.2: Fundamental TM mode intensity and refractive index of a dielectric waveguide [9]. Notice InGaAs layers are placed between active region and cladding layers to increase refractive index contrast and the confinement factor.

Γ is defined to quantify this point:

$$\Gamma = \frac{\int_{active} E_z^2(x,z)dxdz}{\int_{spzce} E_z^2(x,z)dxd} \tag{3.10}$$

The overlap factor is crucial for obtaining a low threshold current density.

In dielectric waveguides, the thickness of the cladding scales linearly with wavelength, and the doping required to support electrical transport will create a loss that increases at λ^2. This causes trouble for mode confinement for wavelength longer than 10 μm. One approach is to manipulate surface plasmon mode, where the cladding is now metal with a negative dielectric constant. The loss of a single plasmon waveguide can be written as (for detailed derivation, please see [102] pp. 96):

$$\alpha = \frac{4\pi n_m {n_d}^3}{{k_m}^3 \lambda} \tag{3.11}$$

where n_m, k_m are the real and imaginary parts of metal's refractive index, while n_d is the refractive index of dielectric's. n_m and k_m approximately scale linearly with wavelength, which makes loss decrease with λ. The mode intensity profile and

schematics of surface plasmon waveguide used on a QCL lasing at 11.2 μm [10] is shown in Fig 3.3. The overlap factor Γ is calculated as 70%, much higher than that (54%) of a reported device with similar active region thickness [109].

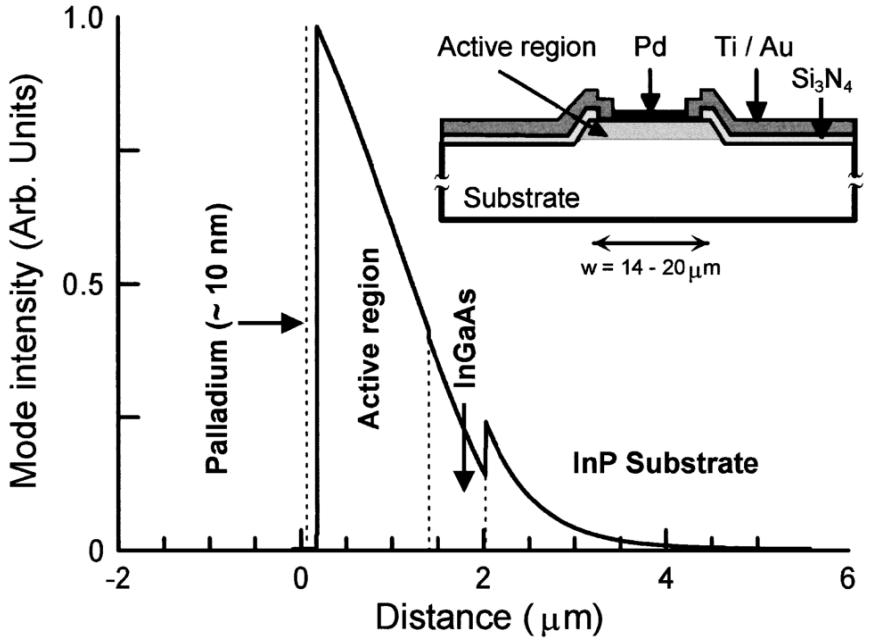

Figure 3.3: Mode intensity profile of a surface plasmon waveguide [10]

It is worth mentioning that surface plasmon mode is widely used in THz QCLs, due to the much longer wavelengths for those devices. The early demonstrations of THz QCLs was reported with single [110] and double surface plasmon waveguide [75], and later on with metal-metal waveguide [111].

The refractive index of cladding layers are tuned by changing the doping levels, they can even be negative with very high doping level [75]. The relationship can be derived through a Drude-like approximation approach [102]. There is another type of waveguide that manipulates the doping level of cladding layers and surface plasmon mode for efficient mode confinement. This type of wave guide is called plasmon enhanced waveguides, [112, 11]. By higly doping the top layer in contact with the metal, the strong decease of the refractive index in that layer will 'push' the mode into the core region, enhancing cofinement (as shown in Fig. 3.4). They can also use the interaction between the lossy plasmon mode and the fundamental mode to tune the dispersion of the fundamental mode [11].

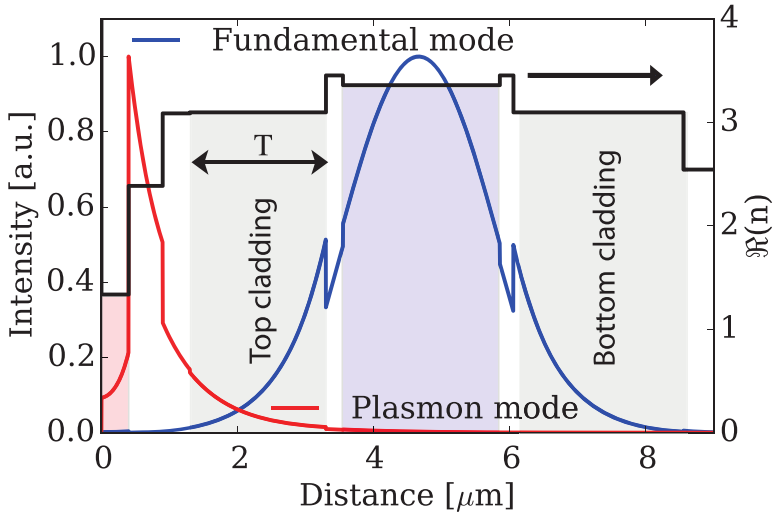

Figure 3.4: Mode intensity profile of a plasmon enhanced waveguide [11]. Red curve on the left indicates plasmon mode, blue curve on the right indicates fundamental mode. Note the overlap between plasmon mode and fundamental mode, by changing the top cladding thickness the overlap between two modes will be changed, then tuning the dispersion.

3.1.2 Lateral Confinement

The fabrication of laser ridges creates the lateral confinement for the radiation. It usually has a larger scale than the vertical confinement in the growth direction, due to the resolution difference between the MBE/MOVPE and dry/wet etch process. The dimension of laser ridges varies from several microns to tens of microns, the optimum width for a specific device should be picked with consideration for power, mode selection and confinement.

There are two most common lateral waveguide geometries used in QCL devices: simply-etched laser ridge and buried-hetero structure.

In the conventional laser ridge structure (as shown in Fig. 3.5), the lateral waveguide is achieved by etching through the cladding and gain media, followed by deposition of insulation layer (Si3N4/SiO2) and top contact metal. Insulation layer is not necessary if electrical insulation is not needed. As desribed in the following chapter, device fabricated and presented by the author does not have the insulation layer, all the devices is bonded to electrical bias port on the top of the ridge by indium bonding.

As shown in Fig. 3.5, there are two ways of shaping the lateral waveguide struc-

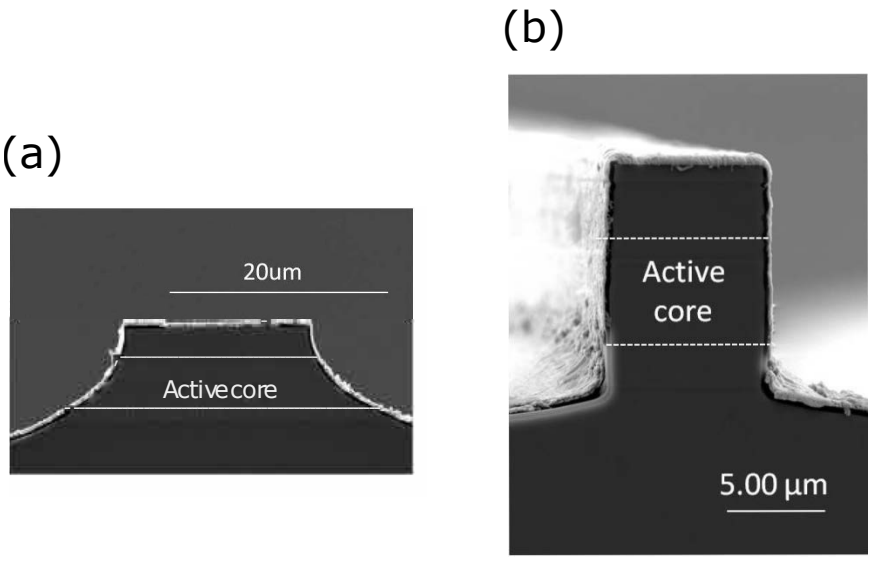

Figure 3.5: (a) SEM image of the cleaved facet of a 24 μm wide wet-etched laser ridge. (b) SEM image of the cleaved facet of an 8 μm wide dry-etched laser ridge. [12]

ture: wet etching and dry etching. From the author's experience (see next Chapter), wet etch will produce a smoother sidewall surface as compared to dry etch, but the sloped side wall that wet etch produces enables the coupling between the TM mode and the lossy surface plasmon mode in the insulation layer [12], which increases the waveguide loss. Besides, the mode confinement factor is lower in wet-ethced ridges because the transverse mode goes deeper into the substrate [12]. In most cases, with the same gain media, dry-etched ridges will have a lower current threshold.

That being said, even wet-etched simple ridge geometry provides a very good mode confinement ($\sim$70% for a proper ridge width [102] pp. 101), due to the huge difference in refractive index between the active region and the insulation layer (air if insulation layer is not deposited). Fig. 3.6 shows the simulation result of a simple ridge waveguide using Comsol. The device simulated here is a wet etched QCL ridge waveguide lasing at $\lambda \sim 10\mu$m.

One variation of the simple laser ridge geomoetry is the so-called double channel geometry (shown in Fig. 3.7). As compared to the conventional laser ridge, where all the material between two laser ridges are being removed, this geometry only etches away material in the two *channels* that defines the laser ridge. The fact that only the

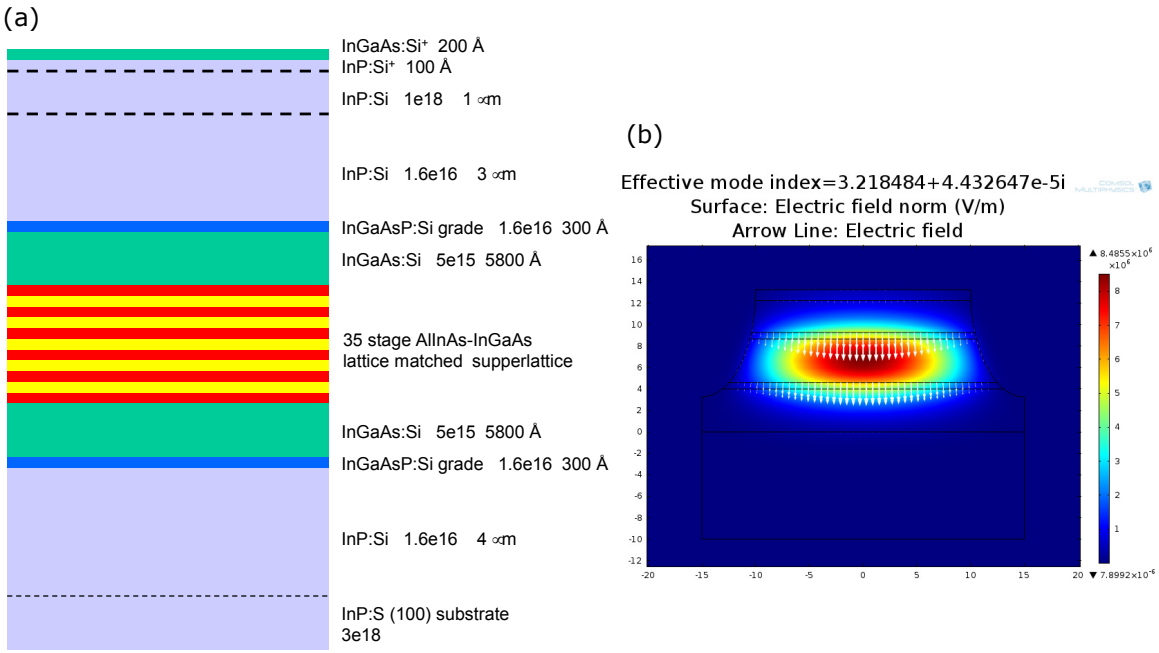

Figure 3.6: (a) Waveguide growth structure for a device lasing at 10 μm (wafer from Nanyang Technological University, Prof. Qijie Wang's group). (b) Mode profile of a fundamental TM mode for a 20 μm ridge etched 10 μm, $\Gamma = 76.3\%$.

minimum amount material is removed gives double channel geometry a much larger contact surface area when epi-down mounting (will be discussed in the next section) is used for the device, hence a better heat removal performance.

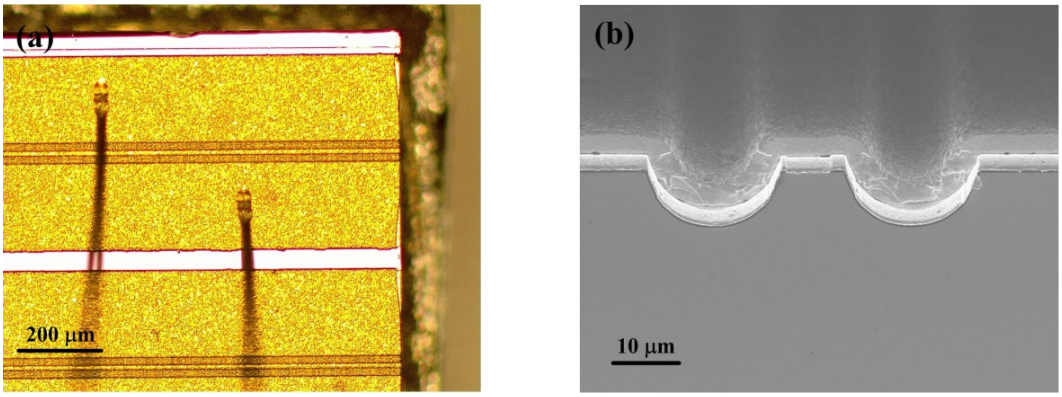

Figure 3.7: Fabricated CW ridge lasers in double channel geometry [13]. (a) Microscope image of the fabricated array. (b) SEM image of the output facet.

Other than the simple ridge geometry, another approach is called buried heterostructure waveguide. For this type of waveguide, after the initial etching, a layer of semi-insulating, thermally-conductive InP is regrown on the sidewalls (Fig. 3.8).

This regrowth is usually done by metal-organic chemical vapor deposition (MOCVD) and it provides both optical and electrical confinement.

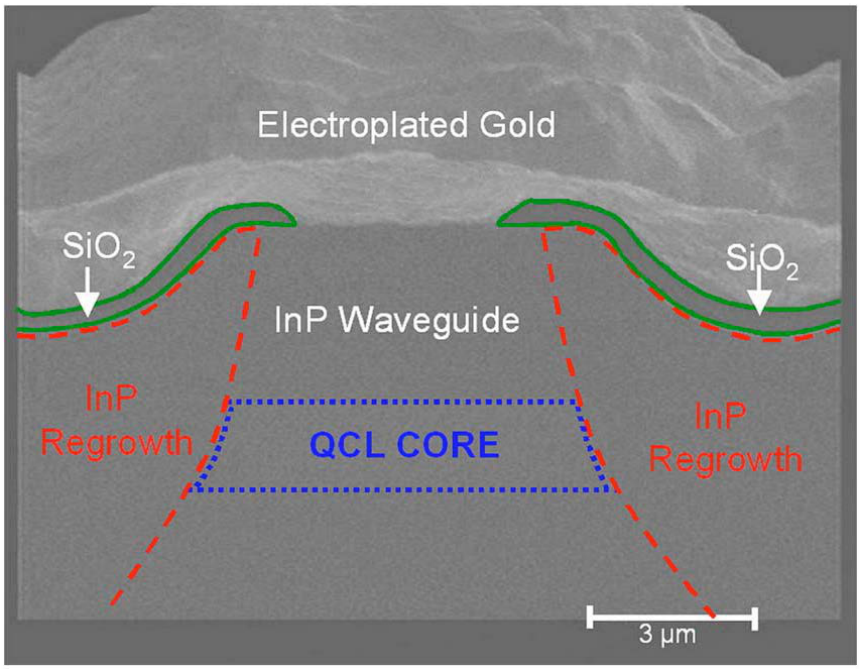

Figure 3.8: Cross-section SEM image of a 6μm wide buried heterostructure QCL. The QCL core is clearly visible in the center of the image surrounded by regrown InP material. The regrown interfaces are highlighted by dashed lines. The sample is also capped with electroplate gold. [14]

As compared to simple ridge waveguide with electroplated gold, buried heterostructure waveguide sandwiched a regrown InP layer between the laser core and gold layer. Since the lattice constant and coefficient of thermal expansion for the regrown InP matches that of the gain medium (InGaAs/InAlAs), the stress on the device can be significantly reduced [34]. While gold has a thermal expansion coefficient almost three times that of InP ($14 \times 10^{-6}K^{-1}$ for gold as compared to $4.6 \times 10^{-6}K^{-1}$ for InP), which will contribute to significant thermal stress in packaging at high temperatures.

Given the huge thermal advantage buried heterostructure can provide, regrowth step alone makes the process challenging and time-consuming.

3.2 Mounting Techniques

The development of mounting techniques has been constantly pushed forward by the pursuit of CW mode operation. For a typical operation of a LWIR QCL device, with a current density of 3 kA/cm^2 under an applied electric field of 100 kV/cm, the power generated per unit volume will be as high as 3E8 W/cm^2. This is 10-100 larger than that of interband devices and will melt not only the device but the mount if not dealt with properly.

There are two basic types of device mounting: epi-up mounting (epilayer-up, epitaxial side up, junction-up) and epi-down mounting (epilayer-down, epitaxial side down, junction-down). For epi-up mounting, the device is facing up in growth direction, while the bottom of the device is in contact with a heat sink (usually copper). In between the device and the heat sink, there is usually a layer of indium to improve the contact at the interface and facilitate thermal transport. For epi-down mounting, the device is usually coated with electroplated gold and then mounted facing down to a patterned submount (AlN, gold, diamond) with indium or Au:Sn (80:20) solder [113]. The submount along with the device will then be mounted on a heat sink (Fig. 3.9). Being in direct contact with the heat sink, the epi-down mounting greatly improved the heat removal of the device.

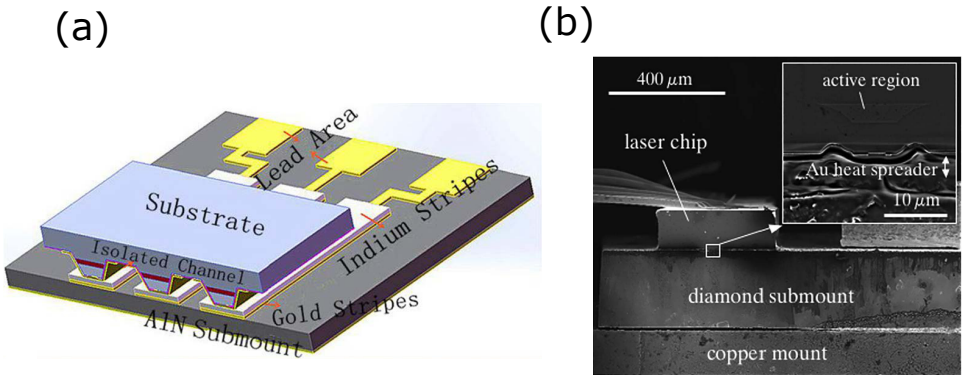

Figure 3.9: (a) The shcematics of a QCL array epilayer-down bonded on a AlN submount [15]. Indium is used to facilitate good thermal contact and thermal conductance. (b) SEM picture of the facet of an epi-down on diamond mounted QCL chip. Inset: Close-up view of buried hetero structure and Au heat spreader soldered to the diamond submount. [16].

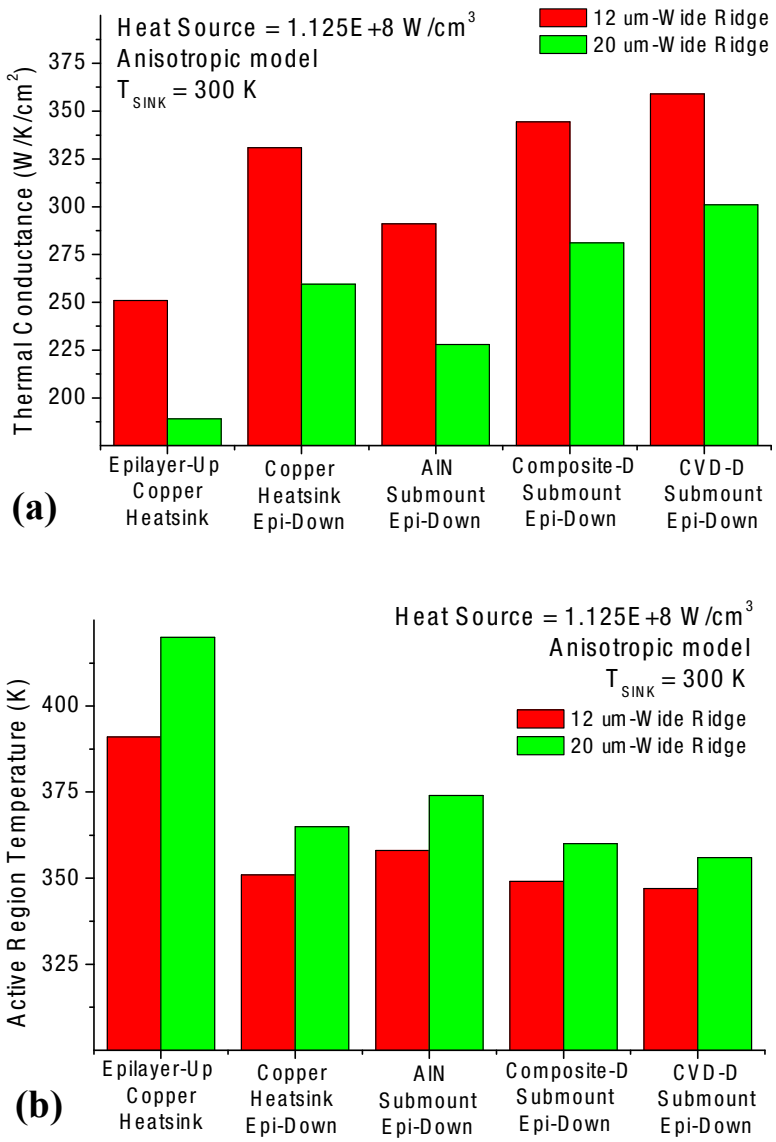

Figure 3.10: Comparison of (a) thermal conductance and (b) core temperature for epi-down bonded QCLs with 3 mm electroplated gold on AlN, composite diamond, and CVD diamond submounts compared to copper heatsinks. [17]

While it is true that the first CW demonstration of LWIR QCL was done on a epi-down mounted device, epi-down mounting is no longer a necessary condition for CW mode operation. Multiple literatures have reported CW mode operation of LWIR QCLs with epi-up mounted devices [114, 115]. The electroplating gold, on the other hand, is essential to the CW mode operation.

For epi-down mounting, there are four different types of submounts (in the case of copper, ther is no submount since the device will be directly bonded to copper heatsink) that can be considered: copper (385 W/K/m2), AlN (170 W/K/m2), composite diamond (W/K/m2), CVD diamond (1800 W/K/m2). A comparison has been done on these submounts based on a Comsol simulation [17], the results are shown in Fig. 3.10.

As the comparison shows, the effect of the submount grows with ridge width. It is also clear that the submount with higher thermal conductance will produce better thermal dissipation. Given that direct epi-down bonding on copper is practically impossible, and the price of diamond wafers are quite high, AlN turns out to be the most economical choices out of all 4 materials.

3.3 Mode Control

Single-mode narrow-linewidth broadly tunable mid-infrared lasers are desirable for highly-selective and highly-sensitive spectroscopic applications. There are two separate goals involved in the statement: single mode emission and wavelength tunability.

Single mode operation can be achieved by introducing gratings into the device. Gratings can be integrated with the waveguide to create a distributed feedback (DFB) QCL (Fig. 3.11.a) [33], or etched into a section directly adjacent to the Fabry-Perot (FP) cabity to form a distributed Bragg reflector (DBR) (Fig. 3.11.b) [19].

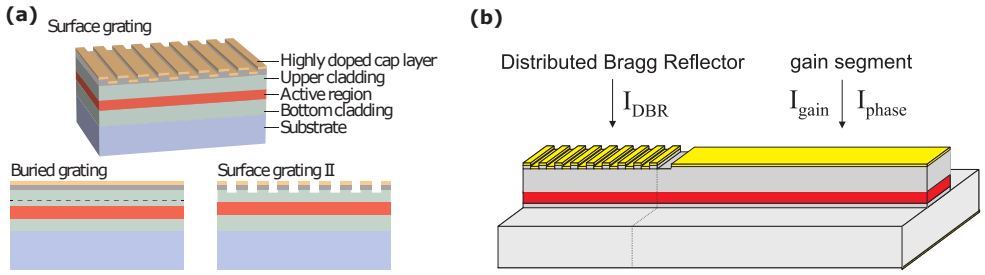

Figure 3.11: (a) Schematic of different types of DFB grating structures [18]. (b) Schematic of DBR structure [19].

For DFB QCLs, the most common ways to introduce gratings into the waveguides are: a surface grating in the highly doped layer [20], as shown in Fig. 3.11.a top and Fig. 3.12; or buried grating sandwiched between the core and cladding layer [114], which requires regrowth after the grating is defined, as shown in Fig. 3.11.a bot left and Fig. 3.13. A DFB QCL with lateral grating has also been reported [116].

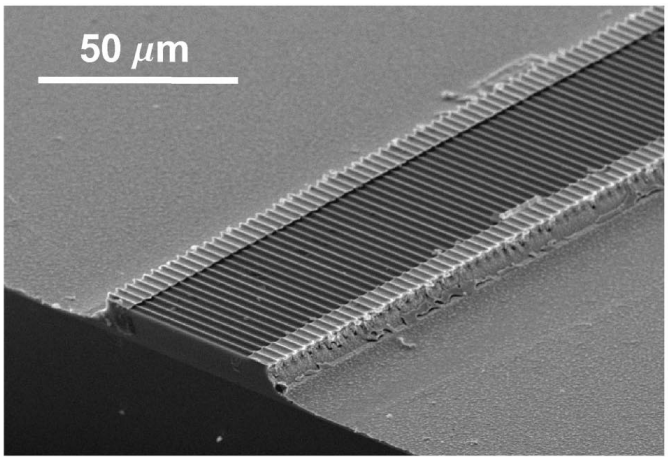

Figure 3.12: SEM image of a DFB QCL with surface grating at the top cladding and a lateral injection scheme [20].

Wavelength tuning can be achieved on single mode devices by changing the operation temperature, which will change the refractive index of the core region. Tunings based on this mechanism is limited to less than tens of wavenumbers ($\sim$10–20 cm^{-1}) [33, 114, 20, 19].

In order to achieve a wide tuning range for single mode QCLs, external cavity

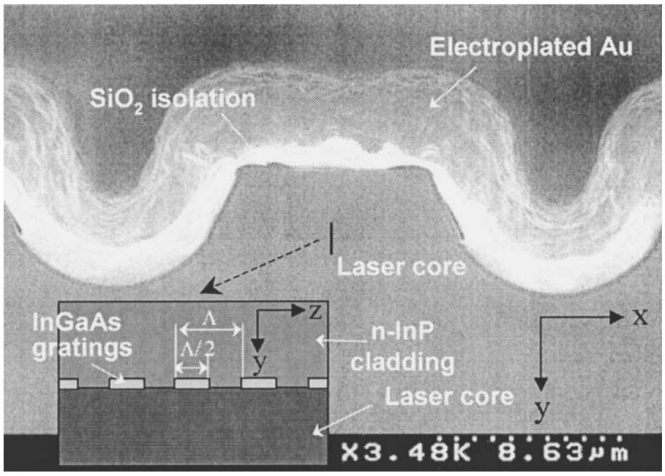

Figure 3.13: SEM image of a cleaved facet end of a DFB QCL with buried grating structure and schematic cross-sectional view through the laser waveguide and grating

(EC) was introduced and has been reported with a tunability in excess of 200 cm^{-1} (Fig. 3.14.b) [117, 16]. Grating tuned external cavity QC lasers (EC-QCL) was usually implemented in a Littrow configuration setup [118] (Fig. 3.14.a).

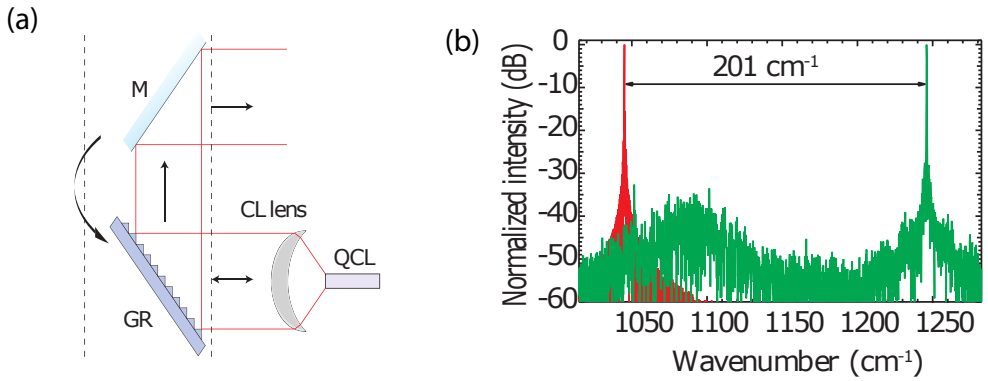

Figure 3.14: (a) Schematics of Littrow external cavity configuration [21]. (b) Spectra of a continuous wave heterogeneous EC-QCL with a tuning of range of 201 cm^{-1} [16].

Though remarkable improvement in tuning range has been demonstrated through EC-QCL devices, one major draw back for this type of devices was the poor side-mode suppression ratio in pulse mode , which can be suppressed by CW operation [119]. The other concern for EC-QCLs is the instability of the mechanical parts involved, which make them vibration sensitive and non-portable. One approach to overcome

this limitation is the utilization of Vernier-effect tuning mechanism, based on which, coupled-cavity QCLs [120] and sample grating QCLs [121] have been demonstrated. A scheme based on two section slot structures was also proposed with a tuning range of 77 cm^{-1} [122].

Chapter 4

Fabrication of LWIR QCL Devices

In this chapter, the fabrication process used for this thesis work will be discussed, along with the problems encountered and the corresponding solutions and optimization to specific steps.

The wet etched epi-up fabrication process has been developed first in details and optimized due to the simplicity and thus quick turn around. Pulse mode devices operated under nitrogen or room temperature can be fabricated in a timely manner for characterization of the gain media. This also allows for the optimization of some basic steps in the process that will be shared in other processes, for example, photoresist coating recipe, exposure time, lift-off metal composition, etc. Afterwards, the epi-down fabrication progress for CW devices was developed. The investigation on dry etch is still in process, still needs to be improved for a better surface quality.

Before we delve into full details, I would like to express my gratitude to our long-term collaborator Dr. John L. Reno from Sandia National Laboratories, for the MBE grown wafers he has been working so hard to provide for this work. Special thanks also goes to Dr. Mykhaylo P. Semtsiv and Prof. W. Ted Masselink from Humboldt University of Berlin for the high quality MBE growth they have provided. I would also like to thank four other research groups from around the globe for providing either MBE grown wafers or fully packaged devices: Prof. Markus Amann's group from Walter Schottky Institute in Technical University of Munich, Dr. Gottfried Strasser's group from TU Wien, Prof. Qijie Wang's group from Nanyang Technolog-

ical University, and Dr. Masamichi Yamanishi's group from Hamamatsu Photonics K.K. The wafers and devices from these groups, whether or not reported in this thesis, has helped tremendously to push forward the development of in-house fabrication capability, the characterization of mid-infrared QCL devices and the demonstration of mid-infrared comb devices.

4.1 Epi-up Fabrication for Pulsed Devices

The fabrication starts with MBE grown wafers provided by our collaborators in Sandia National Laboratories (or other helpful sources). The material system used here is lattice matched InGaAs/InAlAs-InP. Fig. 3.6.a shows a typical sequence of the layer structure. Sometimes, lower cladding is not grown [62]. In that case, the InP substrate will serve as the lower cladding, and the top cladding has to be grown in a Metal-Organic Chemical Vapour (MOCVD) system separately after the MBE growth. But this does not make any difference to the fabrication process.

The wet etch epi-up process can then be summarized into the following steps: a) top contact deposition; b) lift-off; c) ridge pattering; d) ridge formation with wet etch; e) back contact deposition; f) annealing for back contact.

The top contact of Ta/Au 200/1000 Å is deposited with E-beam evaporation, after image reversal photoresist (AZ 5214E [1]) is patterned and developed. After deposition, the sample with patterned photoresis and metal is then soaked in acetone to transfer the pattern to the metal layer. The ridge is formed by either wet or dry etch. For wet etch, we use a conventional positive photoresist as etch mask (SPR 700 [2]). For the photoresist to be used as wet etch mask, a post exposure bake step is added between exposure and development to harden the mask and increase adhesion (see Chapter 4.3 for details). Ge/Au/Ni/Au (20/50/40/50 nm) was deposited with E-beam evaporation as back contact, and was then annealed at 400 C for 30 s in N2 atmosphere to form an ohmic contact.

[1] $http://dvh.physics.illinois.edu/pdf/AZ5214E.pdf$

[2] $http://docs.capitolscientific.com/manufacturer/dow_electronic_materials/datasheets/SPR700_Photoresist.pdf$

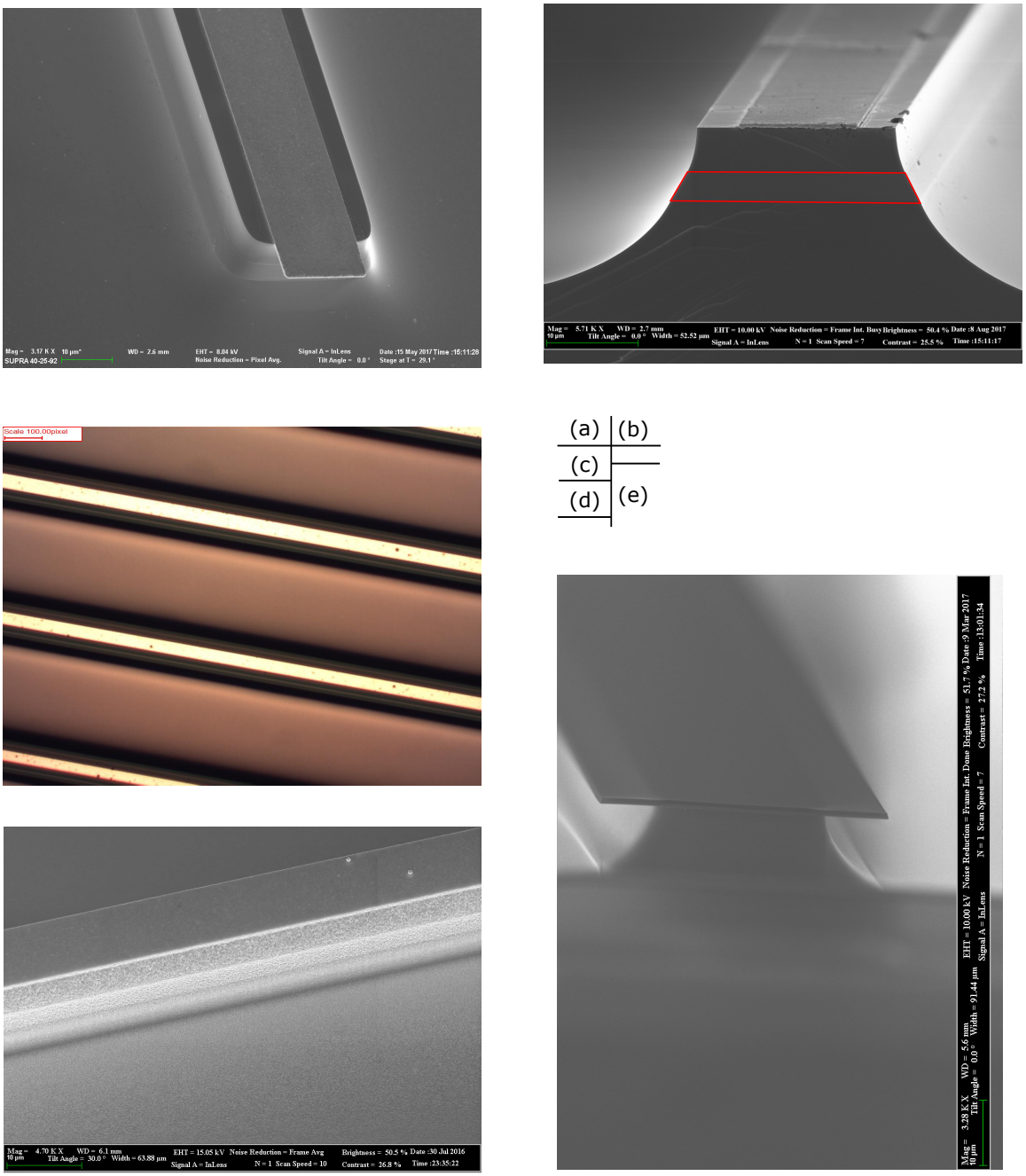

Figure 4.1: (a) SEM top view of a finished uncleaved device. The image shows the undercut from the top contact layer at the end of the ridge. (b) SEM image of a cleaved facet. Highlighted part with lighter shade is the gain media. (c) Optical microscope image of a finished device. Top contact layer has a shiny look due to reflection. (d) SEM image of a dry etched device. (e) SEM image of an unfinished sample with wet etch mask (photoresist) on top. The etch undercut can be seen at both sides of the ridge.

The dry etch process is similar only without step c, because the top contact gold is also used as dry etch mask to define the laser ridge. The conditions currently used for the reactive ion etch (RIE) is: 40 W ICP power, 40 W RF power, 0.2 Pa chamber pressure, 250 C substrate temperature and gas flows of 3.0/0.53/11.0 SCCM for BCl_3, $SiCl_4$ and Ar respectively. The etching rate is about 0.125 μm/min. Images of finished as-fabricated device and steps in between are shown in Fig. 4.1.

The device is then cleaved (1-4 mm in length) and mounted onto copper submount, epi layer facing up. Thin indium strip is used to bond the top contact layer to a chip carrier, where a copper wire is soldered to establish electrical connection.

4.2 Epi-down Fabrication for Continuous Wave (CW) Devices

As mentioned in Chapter 3, epi-layer down mount is desirable for QCL device to operate in CW mode at room temperature. And CW operation will produce a better comb performance with a narrower beatnote in the RF domain. DFB gratings [18, 33] or chirped gratings can be introduced into the cap layer for single mode devices, or comb devices. In the development of epi-down devices, double channel geometry was implemented for the improvement of heat removal and the mechanical stability that it provides.

The epi-down process can be summarized into following steps: a) grating patterning; b) grating etch (dry [123] or wet [124, 33]); c) double channel patterning; d) double channel etch; e) insulation layer deposition; f) window opening; g) top contact deposition; h) lift-off; i) Au electroplating; j) backside metalization; k) annealing.

Before backsie metalization, lapping can be done to thin down the device to further increase the heat removal. But since the majority of the heat will dissipate through top contact with electroplated gold, plus the complexity lapping will introduce, this step is not done for this work. A flow diagram [13] of the CW epi-down device is shown in Fig. 4.2 (for the simple ridge configuration and without top grating etch).

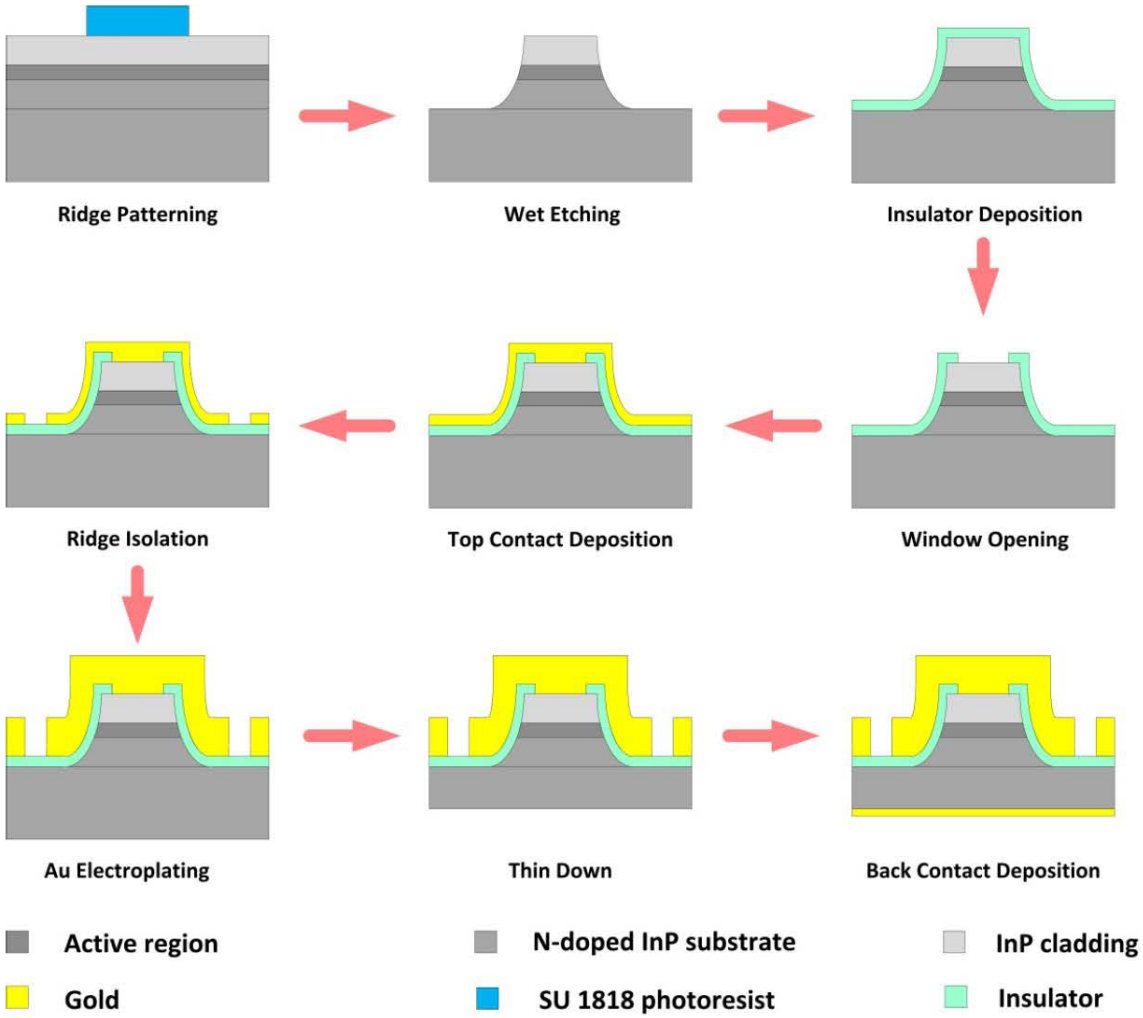

Figure 4.2: Flow diagram of the CW fabrication process [13].

The grating is determined by $\Lambda = \lambda/2n_{eff}$. For a typical mid-infrared QCL lasing at 10 μm with $n_{eff} = 3.2$, a grating period of $\sim 1.5\mu$m is needed. Such feature requires very high resolution ($\sim 0.1\mu$m). Hard contact lithography [33], E-beam lithography [114], and hololithography [124] techniques have been implemented to define the top grating. The grating etch can be done using either RIE [123] or chemical wet etch [124, 33]. After the waveguide etch, a 450 nm SiO2 layer is deposited in a CVD chamber, serving as the insulation layer between the sidewall and later-on-deposited gold.

Thick photoresist (AZ4620) need to be used to pattern the window on the SiO2 layer if the double channel is etched deep (> 5 μm). Since thinner photoresist with

low viscosity (SPR700) will suffer from severe edge effects at each channel and will not be able to cover the sharp corners. This will lead to inconsistent coverage of the insulation layer after etching and hence short the device.

As can be seen in the flow diagram, for CW device, the top contact gold layer is covering the sidewall as well. The gold on the sidewall is crucial since it serves as the seeding layer for electroplated Au to grow on, and the heat removed through side wall serves an important role in CW operation. To ensure the success of electroplating, also to prevent the device from burning by too much current going through one single ridge, a special feature that will electrically connect all ridges together is designed in the mask (shown in Fig. 4.3).

AlN wafer is used as the epi-up submount, Au electrode was deposited and patterned using lift-off. Thin indium strip is placed on top of the electrode to bond the device to the submount. The device can then be mounted epi layer facing down onto the submount. Electrodes on the submount and the back metalization layer can be electrically connected for test purposes.

Images of fabricated epi-down devices is shown in Fig. 4.3. A detailed process is also attached in Appendix A for reference.

4.3 Problems and Optimization

4.3.1 Wet Etch

Due to its great potential for the fabrication of optoelectronic devices [125] and electronics (field-effect transistors [126]), the wet etch technique for InGaAs/InAlAs-InP system has been very well developed and studied.

Basically, wet etch is the physical removal of materials through chemical reaction in solutions. And it falls into two categories: selective and non-selective. A selective etchant attacks one material preferentially to others in a heterostructure. While a non-selective etchant removes all materials at a similar rate. Selective etch is used when a specific layer of material needs to be removed, and can define special

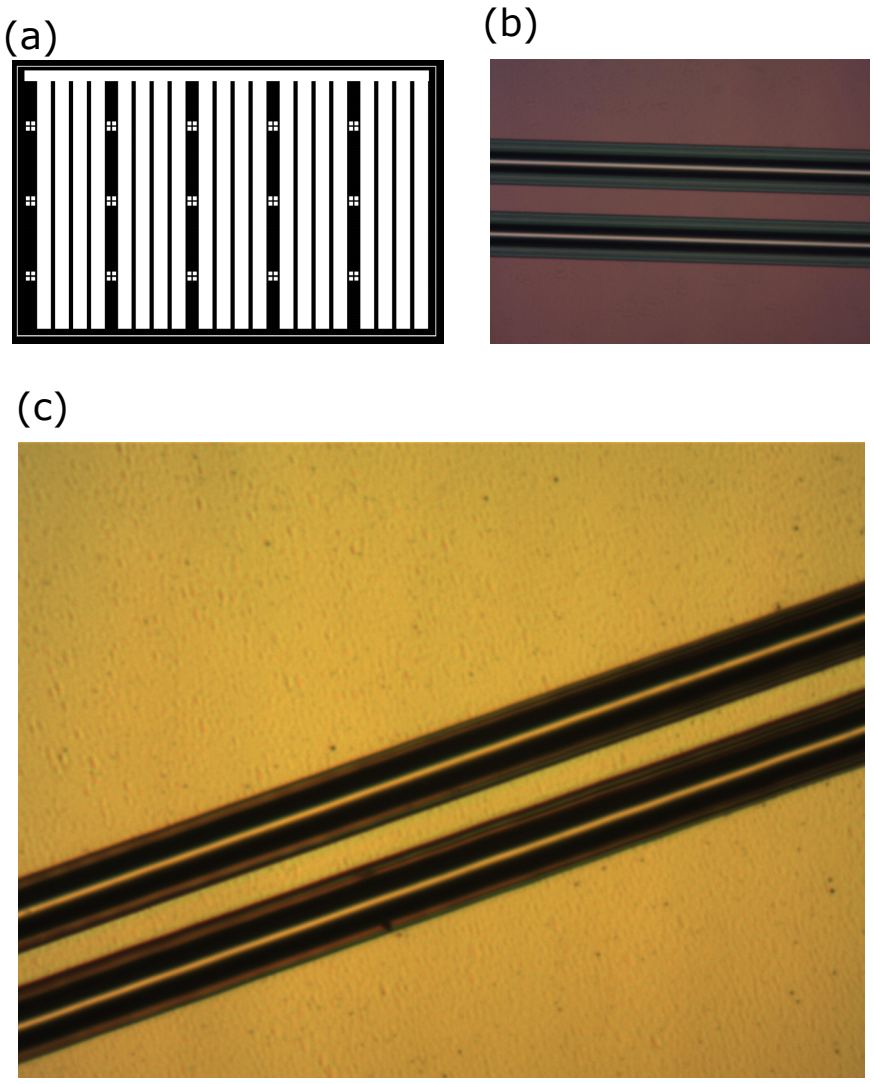

Figure 4.3: (a) Mask design with special feature on top of all ridges that connect them together for electroplating. Geometries in white is the shape of metalization layer. For image reversal photoresist, shapes filled with black will be exposed, and then stay on the wafer for lift-off. (b) Microscope image of an etched double-channel waveguide. (c) Microscope image of an epi-down device after SiO2 window opening and top contact deposition.

three-dimensional shapes. Non-selective etch is useful when a smooth and continuous surface is required.

Strong edge effects have been observed on ridge samples, where the etch rate is insonsistent over the entire wafer. There is also the problem of different etch rates in different directions. Most etchants will etch laterally under the mask and vertically (epi-layer growth direction) at the same time (as shown in Fig. 4.1.a and e). Non-selective are usually more isotropic in nature, which means it has a similar etch rate laterally and vertically, and will have a rounder sidewall profile after etch.

Aonther aspect that needs to be taken into consideration when picking the proper etching recipe is whether this etchant is diffusion-limited (or difusion-controlled) or reaction-limited (reaction-controlled). Diffusion-limited reactions are those that occur so quickly that the rate of the etching is the rate of transport of the etchants through the reaction medium and already patterned structures on the wafer. As quickly as the etchant reaches the material, the reaction happens. On the other hand, the rate of reaction-limited etch is determined not by transport but by how fast the components react. An easy way to tell if this recipe is diffusion-limited or reaction-limited is to test whether the etch rate is affected by stirring or agitation. Selective etchants are often reaction-limited and may be more anisotropic. Table 4.1 contains a list of common etchants (selective and non-selective) for the InGaAs/InAlAs-InP material system.

For the fabrication in this work, the etchant HBr:HCl:H2O2:H2O (10:5:1:50) is used. An etch rate of $\sim$1 μm/min is observed on MBE grown wafers, while the etch rate from different growers, even with the same layer structure, can be different. So a test etch to characterize the rate is crucial prior to processing any new wafers. Different etch rates has been observed with and without agitation (moving sample holders), which proves the diffusion-limited nature of this etchant. And a wide range of lateral etch ratio (vertical etch/lateral etch) has been observed from 1.2 to 1.8, mainly related to different mask geometry. Double channel geometry has a lower ratio as compared to single waveguide geometry.

When mixing the solution, H2O2 has to be added the last, and acid has to be

Etchant	Type	Etch Rate (μm/min)	Comments	References
HBR : HCl : H2O2 : H2O	Non-selective	$\sim$1 (10:5:1:50)	Compatible with AZ5214 photoresist. Smooth and nearly isotropic.	[114, 127, 128]
H2SO4 : H2O2 : H2O	Selective against InP	0.25-0.35 (1:10:220); $\sim$2 (4:1:1); 0.4-0.7 (1:1:10)	Heats up a lot when first prepared. Use when cooled down to 20 C. Good for precision removal of top InGaAs waveguide in QCLs. Etch rates proportional to Ga and As content.	[128, 129, 126, 125, 130]
1% Br2 : methanol	Non-selective	6-8	Smooth and fast. Not compatible with AZ photoresist.	[128, 131]
citric acid : H2O2	Selective for InGaAs	0.12 (2:1)	Selectivity over InAlAs $\sim$25	[132]
HCl : H3PO4	Selective for InP	$\sim$2.5 (1:1)	Reaction rate limited	[125]
H3PO4 : H2O2 : H2O	Selectie for InGaAs	Various	InGaAs etch rate $\sim$0.4 (1:1:8); InGaAs and InAlAs etch rate $\sim$0.1 (1:1:38)	[133]

Table 4.1: List of several selective and non-selective etchants for InGaAs/InAlAs-InP material system

added to water, not the opposite. Significant color change can be observed after H2O2 is added. It is the result of ions being oxidized. Before dipping samples in, a 20-minute aging period is necessary for the solution to fully mixed up and the oxidation process to finish. During this period of time, the color of the solution will keep getting darker.

For the purpose of patterning the ridges, photoresist is used as etch mask for the process. Different problems can occurr during this process and they are shown in Fig. 4.4. Fig. 4.4.a shows an etched sample with photoresist peeling off during the etch process. The photoresist used here is SPR700. This problem was solved by a post exposure bake (PEB) for 1 min on hot plate after exposure before development. This step hardens the photoresist and increase the adhesion to the substrate to avoid peeling off. Fig. 4.4.b and 4.4.c show images of the top contact gold peeling off during the etching process. This does not occur to all ridges, but was not observed when the

ridges are wider than 20 μm. This reveals that the adhesion of the top contact layer is not strong enough to hold the mechanical force on the photoresist mask caused by the agitation of the solution when the gold contact area is too small (also gets worse when the etch goes deeper because the undercut and the force on photoresist grows with that). In order to increase the adhesion of the top gold layer, before the gold deposition, the sample was put into asher for 5 min to get rid of excess photoresist and then dip into BOE for 15 s for removal of local oxide and cleaning. With these two steps, a good wet etch profile can be obtained, as shown in Fig. 4.4.d.

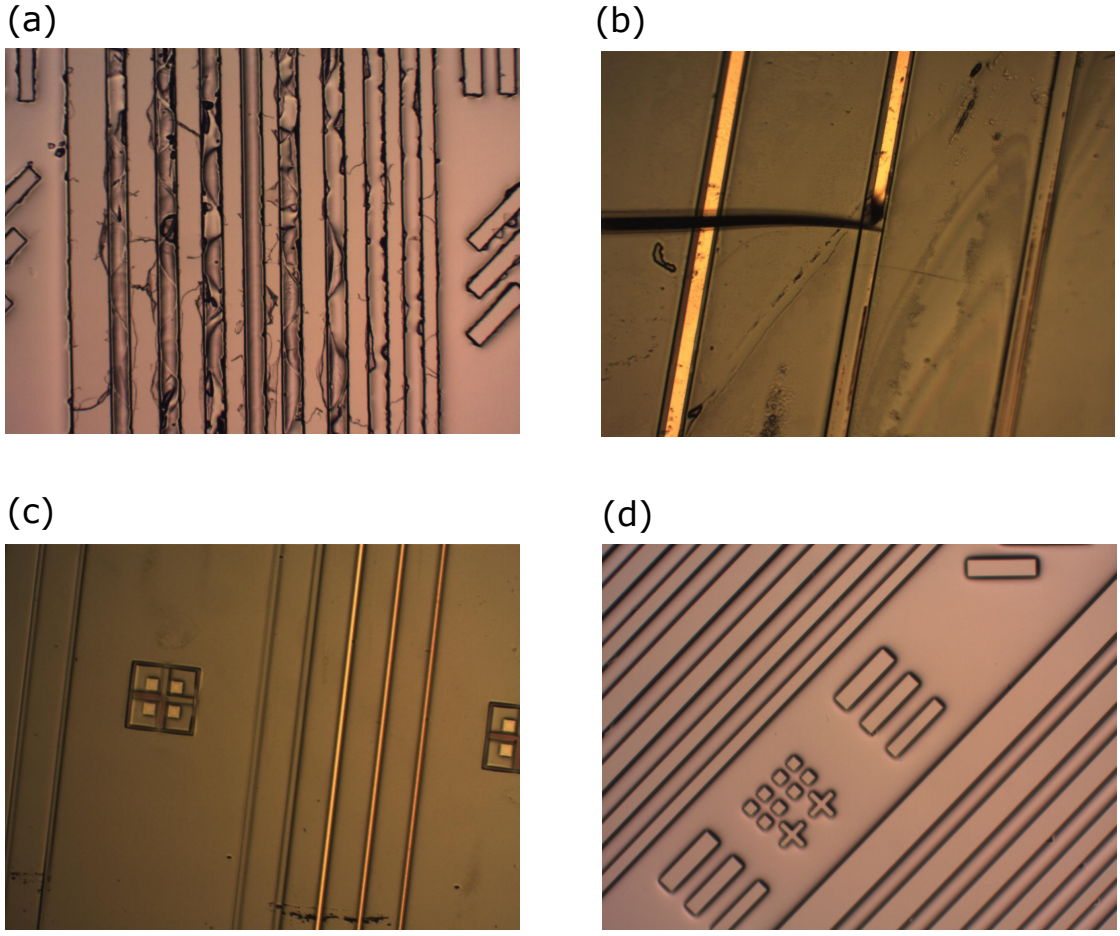

Figure 4.4: (a) Image of an InP sample after wet etch, with photoresist washed away by acetone. The partial damage seen on top of the ridge was caused by peeling off of photoresist during etch process. (b, c) Image of an MBE grown sample with photoresist washed away and gold on top. On some ridges, gold contact layer has completely peeled off with photoresist during the process. While on others, part of the gold is still sticking to the ridge while the other part is detached. (d) Image of an perfectly-etched InP sample after wet etch with photoresist washed away.

4.3.2 Dry Etch

Dry etch is completed through a process called reactive-ion etcching (RIE). RIE uses chemically reactive plasma to remove materials, and chlorine-based (Cl) reactive gases along with other inert gases are usually used for the etching of InGaAs/InAlAs-InP.

An illustration of an Inductively coupled plasma (ICP) RIE system is shown in Fig. 4.5. The ICP source generates a high-density plasma due to inductive coupling between the RF antenna and the plasma. The antenna, connected to the RF souce, creates an alternating RF magnetic field and induces RF electric field. The electrons will be energized and partcipate in the ionization of gas molecules and atoms at low pressure. The chamber walls are protected from erosion or bombardment due to the absence of electric field around them. The reactive ions will react chemically with the material, while the other heavy ions with high kinetic energy (accelerated by the large electric field created by the charge built up on the platter) will contribute to physical etch (sputtering) through direct bombardment. The careful choice of RF and ICP power is very important and sometimes a trade-off between quality and etch rate. The combination of chemical etch and highly-directional bombardment can produce very anisotropic etch profile.

Highly vertical etch has been demonstrated on InP/InGaAsP in Cl2/H2/Ar inductively coupled etching [134]. While etching with Cl2 gas is able to produce smooth sidewalls and a high selectivity aginst mask materials like SiNx and SiO2, it has suffered from large undercut or slow anisotropic etch rates. Additive gas is used to remedy those problems, including Cl2/Ar, Cl2/H2, Cl2/H2/Ar, Cl2/O2, Cl2/N2, and Cl2/BCl3/N2. Adding Ar to the chemistry benefits etch anisotropy due to the increased bombardment from Ar-ion. A novel ICP RIE process utilizing BCl3/SiCl4/Ar has been reported for the etch of vertical nanowire InGaAs MOSFETs [135, 136]. This approach combines the directional BCl3/Ar plasma with low anisotropy SiCl4 chemistry [136] to obtain a vertical etching profile. Where BCl3/Ar alone will only produce a tapered sidewall, and the lateral etch introduced by SiCl4 will compensate for that to produce a vertical side profile.

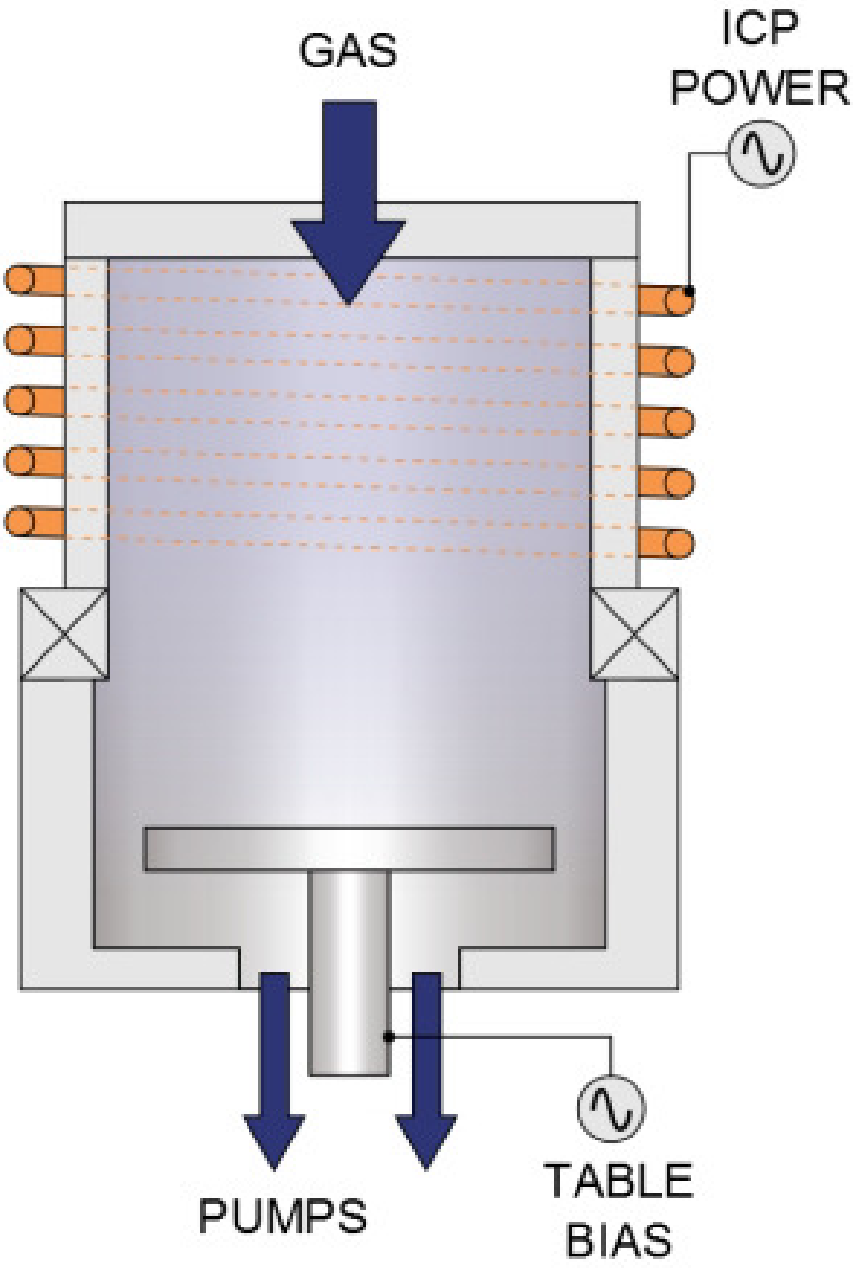

Figure 4.5: Illustration of an ICP RIE system. (image obtained from Oxford Instrument, https://www.oxford-instruments.com/products/etching-deposition-and-growth/plasma-etch-deposition/icp-etch)

We use the recipe reported in [135] as a starting point and optimize the recipe for our purpose. The temperature 250 C and chamber pressure of 0.2 pa remain unchanged, while the gas composition and RF/ICP power has been tuned iteratively for better results. The changes are necessary because top contact layer is used directly as a dry etch mask, which is quite different from what was reported originally (hard mask like SiO2). The physical dimension and material composition is also quite different.

Higher ICP power will increase both Cl radical and Ar ion concentration, hence both chemical and physical etch will increase. This will of course increase the etch rate, but will also lead to worse side wall profile and mask selectivity. Which can be remedied by reducing RF power and decreasing Ar or Cl concentration in the gas.

While the dry etch recipe has not been finalized and still have plenty of room for improvements, promising results have been obtained. Fig. 4.6 shows the SEM images of some processed samples. The optimization process starts with InP pieces and then moved to real MBE grown wafers. Fig. 4.6.a and b show proessed pieces with optimized gas mixture of BCl3/SiCl4/Ar 3/0.53/11 SCCM, with RF/ICP power of 40/120 W. Although small grass structure appears on the substrate, and tiny dots on the contact layer shows that it has suffered from bombadment, the structure in general show no undercut and a smooth, straight sidewall. So this recipe was adopted as the starting point for the processing of real MBE grown sample. Fig. 4.6.c and d show zoomed in and out SEM images of the same piece processed with the previously mentioned recipe on InP. Relatively smooth sidewall can be obtained and no micro grass can be seen. But as partially shown in c and more clearly visible in d, top contact metal has been sputtered and cover the wafer surface around the ridge. This shows too much bombardment happens during the etch and Ar ion concentration should be decreased. Fig. 4.6.e and f shows the results of the sample etched with a lower ICP power with RF/ICP 40/40 W. Top contact gold sputtering is avoided, but sidewall quality has dropped significantly, top contact layer is still bombarded, micro grass structure has appeared everywhere on the etched surface. This is a sign of not enough Cl radical, and bombardment issue still exists. For the future optimization

work, the concentration of BCl3 and SiCl4 should be increased to enhance chemical etch in the process, and Ar gas concentration should also be reduced to decrease bombardment.

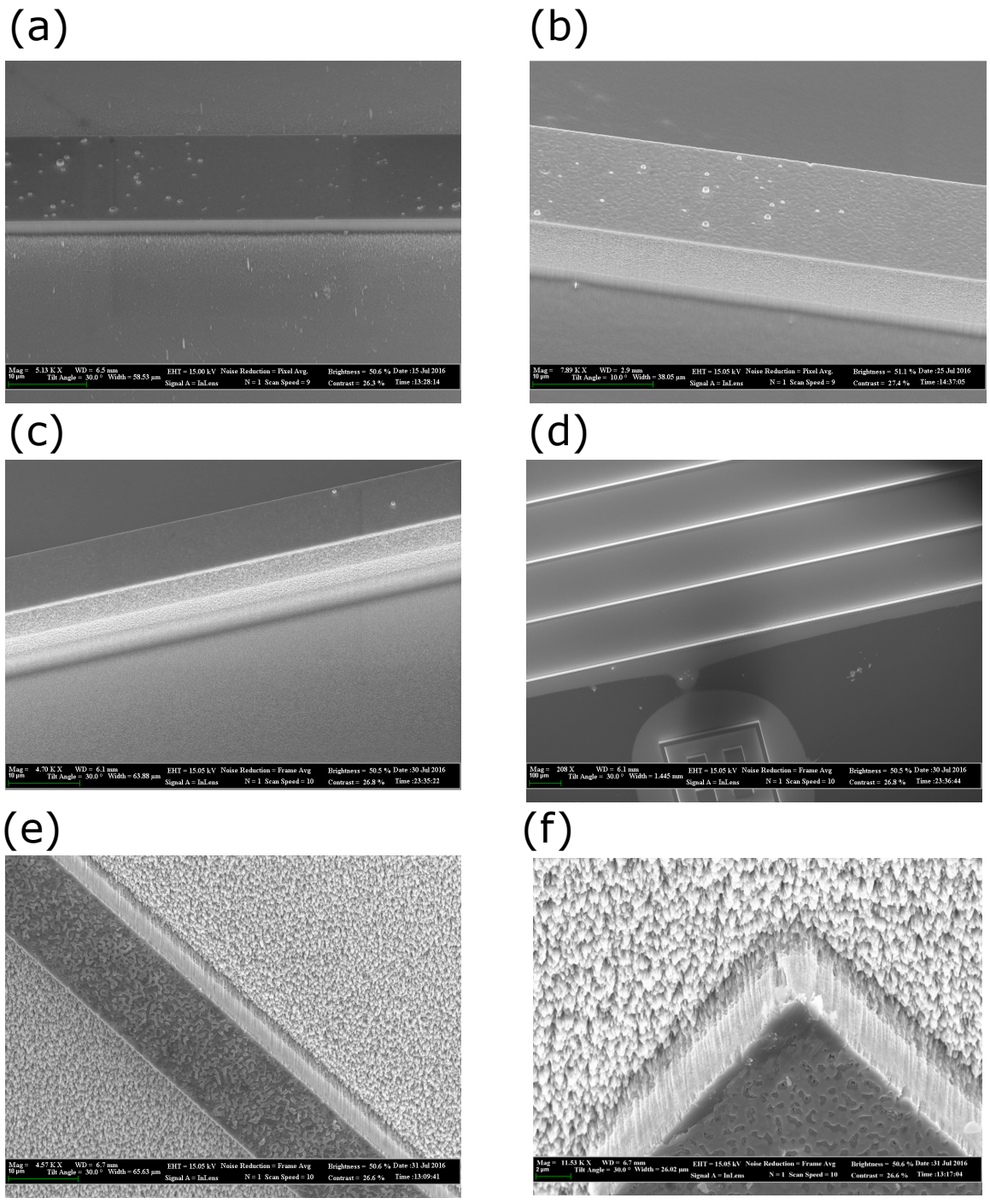

Figure 4.6: (a, b) SEM image of processed InP test samples. (c, d) Zoomed in and out SEM images of processed MBE grown sample. Top contact has been sputtered around the ridge area. (e, f) SEM image of processed MBE grown wafer with lower ICP power. Damage on top contact layer still exist and sidewall profile decreased.

Chapter 5

Characterization of LWIR QCLs and Frequency Combs

Quantum cascade lasers performances are to be characterized after a relatively long chain of processes, starting from MBE growth, all the way through fabrication to mounting. Along this process, different characterization techniques can provie valuable information about the device, including X-ray diffraction (XRD), secondary-ion mass spectrometry (SIMS) and transmission electron microscopy (TEM) for MBE growth characterization, microscope and scanning electron microscope (SEM) for fabrication quality control and optimization. However, there is a lack of direct probe to the performance of the MBE grown structure. This makes it very important to carefully characterize the electrical and optical properties of the final QCL device. In this chapter, we will discuss the experimental setup and present results on multiple QCL devices.

The characterization results reported in this chapter is largely a result of Dr. David Burghoff's hard work, who established the major parts of the experimental setup, assembled the home built FTIR and guided the author to run experiments. The work of division goes as follows: the fabrication of QCL devices is done by the author, so are the basic electrical and optical characterization (IVL curve, spectrum); Dr. David Burghoff conducts most of the comb characterization work, with the author's assistance on the side.

5.1 Experimental Setup

5.1.1 Basic Electrical and Optical Characterization

The QCL device is biased with pulsers from Avtech Electrosystems Ltd. In most cases, MBE layers of gain media are grown in a way that the bandstructure are properly aligned with a higher electron energy on the top of the gain media. This means QCL devices should be biased negatively (with annode on top contact), if no flipping of the dvice occurs in the fabrication process (for instance, THz QCL metal-metal waveguide). Some pulsers are able to bias with either polarity, some with only one. In those cases, inverter could be used to switch the polarity. The pulse width are usually several hundred nanoseconds, with the duty cycle ranging 0.1% to 5%. To prevent overheating, devices are biased in low duty cycle and short pulses.

The electrical signals on the device is detected by voltage and current probe connected to a PC oscilloscope, which then transferred the data to PC for monitoring and processing purposes. Optical signal is detected with a Mercury Cadium Telluride (MCT) detector, whose peak response wavelength is $\sim$14 μm. The signal from MCT is amplified by locked-in amplifier with the sync signal from the pulser, and then transferred to PC through GPIB connection.

Beam from QCL device is collimated and focused onto the detector element with either ZnSe lens or off-axis parabolic mirrors (OAP). Rough alignment are done with the help of a CCD camera. Fine adjustment can be done by fine tune mirror positions to achieve maximum light signals on the detector.

IVL measurement are done with the assistance of Labview programs, where the bias are incremented on a set value and the electrical and optical signal value are recrorded at each point.

5.1.2 Fourier Transform Infrared Spectroscopy

Fourier transform infrared spectroscopy (FTIR) is used to obtain lasing or electrical luminecence (EL) spectrum of the device. FTIR is essentially Michaelson interferome-

ter with one moving mirror controlled by PC, a schematic is shown in Fig. 5.1. When the moving mirror moves, different frequency components coherently or incoherently interfere with each other (different optical path difference for different frequency components), causing detected power to change and producing the interference pattern. The raw data, which is the power in relation to mirror position, is called an interferogram. The interferogram is a scaled version of the Fourier transform of the spectrum.

A Nicolet^{TM} FTIR manufactured by Thermo Fisher Scientific Inc. is used for simple spectrum characterization of QCL devices, while more complicated measurements are done with a lab-built FTIR. The advantage of using a lab-built FTIR is the more flexible manuvering of stage position, alignment, detector and device position, and easier accessibility of data. These are all very desirable for loss and dispersion measurement, and especially for Shifted Wave Interference FTS (SWIFTS) [5].

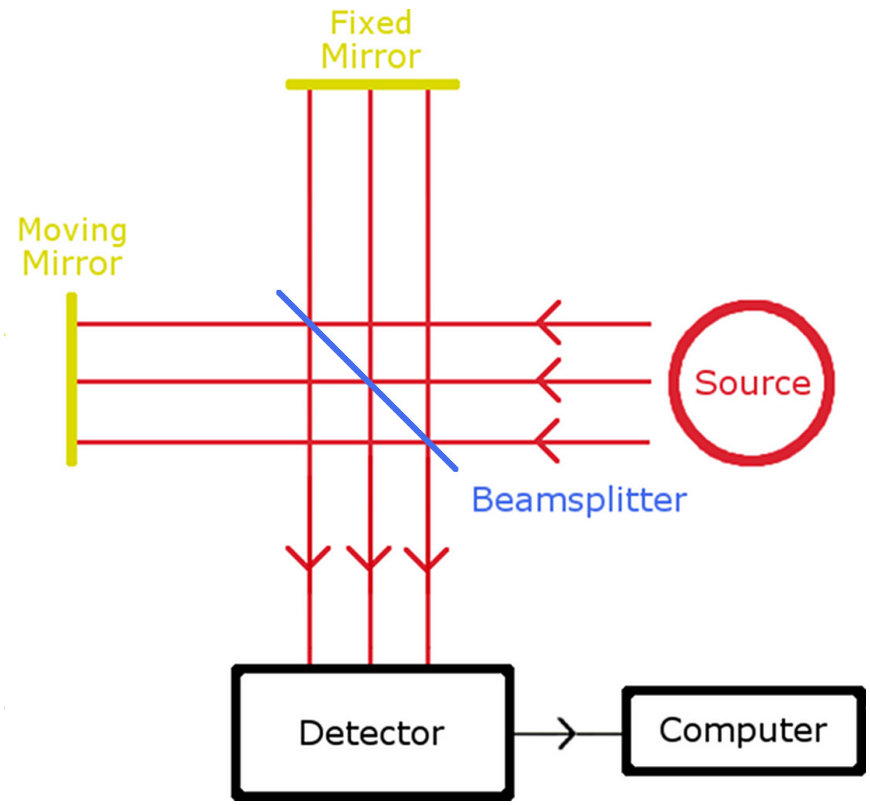

Figure 5.1: FTIR schematic. Light goes through two paths and then combined and shined to a detector. Image taken from [22].

5.1.3 Beatnote Measurement

Coherence is the fixed phase relationship between different sources, it is the most important thing that makes laser a laser. For a frequency comb device, there are two types of coherence: absolute coherence, which is the global phase stability of all lines; and mutual coherence, which is the relative phase stability between any two lines in the spectrum. Absolute coherence is highly-related to the fluctuation of the offset frequency. While mutual coherence is about how even the lines are spaced.

Beatnote can be detected either from the device side or the detector side with a bias tee. It is generated by the beating of adjacent lines in the lasing spectrum, separated by the free spectral range (FSR) of the Febry Perot cavity. For a typical mid-IR QCL device of 3 mm, the beatnote will be around 15 GHz.

Beatnote measurement is a non-rigorous way to characterize the mutual coherence of all the modes in the spectrum. The existence of a narrow beat note does not prove the mutual coherence of all lines, it is possible that a strong pair dominates the beat note. For a rigorous measurement of the phase relation, SWIFTS [5, 137] is required.

For the measurement of the beatnote reported in this work, the signal from bias tee connected to the device is used. Currently, we do not have a working detector that is fast enough for the beatnote measurement from the detector side. We do have several quantum-well infrared photodetector (QWIP) [138], but they have not been properly set up and characterized yet, which will be done in the future. The signal from the bias tee is amplified and then goes through an IQ demodulator, where it is modulated by the local oscillator (LO) signal from a frequency synthesizer. The frequency of the LO signal is picked at a value that is close to the actual beatnote frequency, so the beatnote signal can be downconverted to MHz level, where digital acquisition is possible. For pulsed mode device, in order to increase the SNR of the beatnote measurement, the modulated signal is recorded and narrowed down to the time region where the laser is turned on, the beatnote is then acquired by conducting Fourier transform. The beatnote can also be directly measured by spectrum analyzer. But sometimes, with a weak beatnote, the SNR for pulse mode will be too poor and

the signal cannot be seen on the analyzer. Essentially, all the noise coming from the time when the laser is not on will contribute to the noise and cover the weak signal.

5.1.4 Dispersion Measurement

Group velocity dispersion (GVD) plays a very important role in the formation of comb regimes for both THz [5] and mid-infrared [6].

Before we get into the discussion of dispersion measurement setup, the author would like to delve into the definition of dispersion and the confusion arising from different conventions a little bit. There has been two different conventions in defining a traveling plane wave:

$$E(\omega, t) = E_0 e^{j(-kr+\omega t)} \tag{5.1}$$

$$E(\omega, t) = E_0 e^{j(kr-\omega t)} \tag{5.2}$$

Different conventions have been adopted by researchers from different areas. In this work, we define plane wave as in (5.1). Group velocity is defined as:

$$v_g = (\frac{\partial k}{\partial \omega})^{-1} \tag{5.3}$$

and group velocity dispersion (GVD) is defined as:

$$GVD = \frac{\partial}{\partial \omega}\frac{1}{v_g} = \frac{\partial^2 k}{\partial \omega^2} \tag{5.4}$$

These definition are all correct without confusion, but since the relationship of k and phase ϕ is defined differently, when we are trying to obtain the GVD information from the phase of measurement results, we need to pay close attention. For the definition in (5.1), $k \sim j\phi/r$, so GVD would be:

$$GVD = \frac{\partial^2 (j\phi/r)}{\partial \omega^2} = -\frac{1}{r}\frac{\partial^2 \phi}{\partial \omega^2} \tag{5.5}$$

While for the other convention, it would be:

$$GVD = \frac{\partial^2(-j\phi/r)}{\partial\omega^2} = \frac{1}{r}\frac{\partial^2\phi}{\partial\omega^2} \tag{5.6}$$

For an easy sanity check, keep in mind that group delay (GD) is always positive, because we live in a causal world. Use this to derive the relationship between phase ϕ and GD. Once GD is derived, it is easy to get GVD:

$$GVD = \frac{\partial GD}{\partial\omega}\frac{1}{r} \tag{5.7}$$

As long as the same convention are used along the process, namely measurement, simulation (from the author's experience, Comsol use the same convention as in this work) and design, there will be no problems arising from either convention.

For the dispersion measurement, device is pulse biased slightly below lasing threshold, and the spectrum is measured with home built FTIR. Instead of only recording data from the center peak, the first echo in the interferogram is also recorded. Essentially, the first echo is the pulse signal with one round trip in the cavity, and contains the dispersion information of the devie. The phase of the echo pulse can then be obtained. Using (5.5), GVD can be calculated (use r=2L, where L is the cavity length). With both the center peak and the first echo, one can also derive the group index n_g. It is worth mentioning that the gain and dispersion of THz QCL devices are usually measured with time-domain spectroscopy assisted by integrated THz pulse emitters [139, 140, 141]. It is similar in principle to the approach in this work, essentially the FTIR stage translates the time domain signal to a position dependent signal, scaled by the velocity of the stage.

5.2 Hamamatsu Device

The device described in this section is a fully processed chip shipped directly from Hamamatsu Photonics, with the help of Dr. Masamichi Yamanishi. Fig. 5.2 is

an overview the SEM images of the device. [1] The ridge are 7 μm wide 3 mm in length, dry etched, coated with insulation layer. A window is opened on top of the ridge to make contact, metal contact layer is then deposited, with electroplating gold following. The gain media is a dual-upper state (DAU) design (mentioned in Dr. Kazuue Fujita's thesis [104] and other publications [142, 143]), lasing at 6.8 μm.

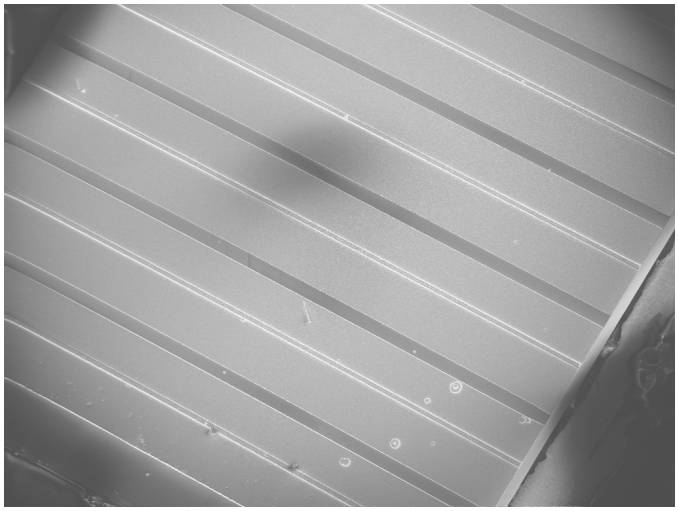

Figure 5.2: Overview of the sample containing multiple devices.

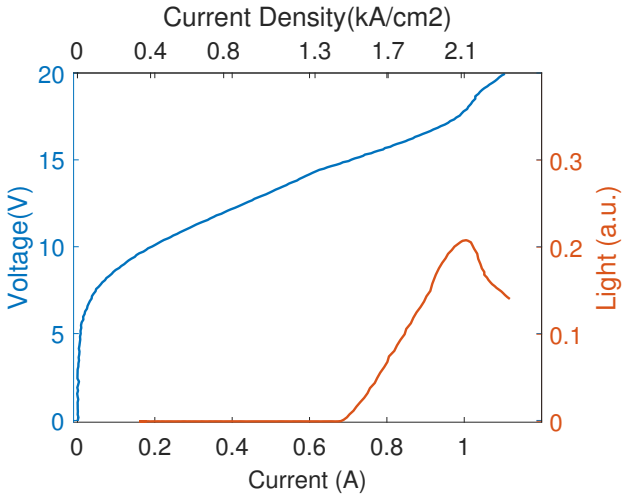

Figure 5.3: Current-Voltage-Light characteristics of the Hamamatsu device.

[1] Details of the sample may be viewed as a trade secret, so SEM images containing too much information on the structure are not presented in this paper. But they are available upon request with approval from Hamamatsu Photonics.

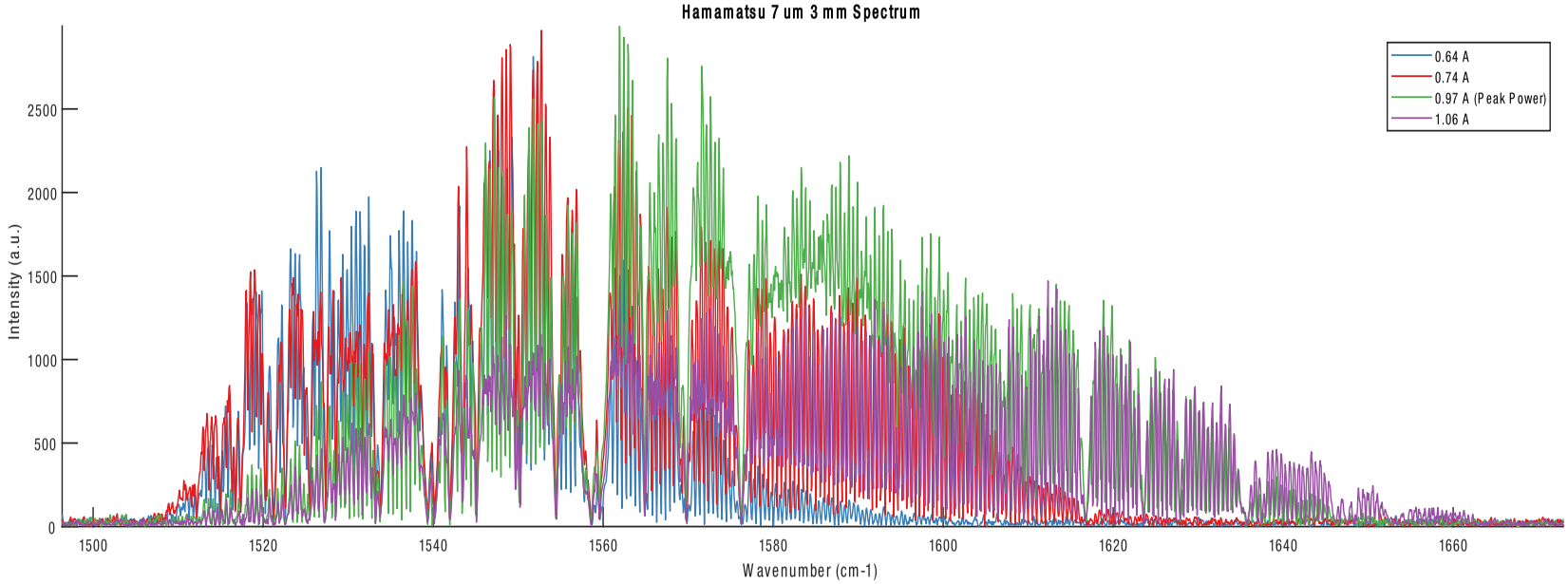

Figure 5.4: Spectra of Hamamatsu device under different biases measured with Nicolet FTIR, at room temperature in pulse mode (20 kHz 100 ns).

Fig. 5.3 shows the IVL characteriristics of the device. The lasing threshold J_{th} is about 3.2 kA/cm^2, and a decent dynamic range of $\sim$ 0.68 A to $\sim$ 0.98 A. A lot of devices got burnt at very low (0.1 %) duty cycles at a farily low current (0.9 A, 4.2 kA/cm^2). Possible explanation is that the insulation layer has not been properly deposited, there might exist some local defects, where the insulation is very thin and electric field is high. When the current goes up, it will burn through the weakest point and burn the whole device. The spectra of the device at different biases at room temperature is measured in pulse mode (20 kHz 100 ns) with Nicolet FTIR and shown in Fig. 5.4. It has a very broad lasing spectrum of around 150 cm^{-1}, which is very promising to have a comb regime. But beatnote measurement shows no sign of the mutual coherence between different modes.

5.3 MIT-NTU Device

The devices mentioned in this section are fabricated in MIT with the MBE wafers provided by Prof. Qijie Wang's group in Nanyang Technological University (NTU). The gain medium gorown on this wafer is a continuum-to-continuum (C-C) design lasing at $\sim$10 μm [23] with a wide (440 cm^{-1}) EL spectrum. The wafer is processed in the previously discussed wet etch epi-up technique, with width ranging from 5 μm to 15 μm.

Fig. 5.4 shows the characterized IVL characteristics of a 15 μm wide 2 mm long device in pulsed operation, in comparison with the reference (25 μm wide 3 mm long) in [23]. The IVL curve and lasing threshold is very similar to the reference, which shows good fabrication quality and characterization.

The lasing spectrum of a 7 μm wide 3 mm long device is shown in Fig. 5.5. The device has $\sim$ 40 cm^{-1} of bandwidth at 300 K.

In order to introduce some dispersion compensation into the laser cavity, a small gold mirror, which servers as a Gires-Tournois interferometer (GTI) mirror, was placed behind the rear facet to reflect light into the facet. In the simplest model for a GTI, light coming out of a partially reflected mirror (QCL rear facet) is reflected at a

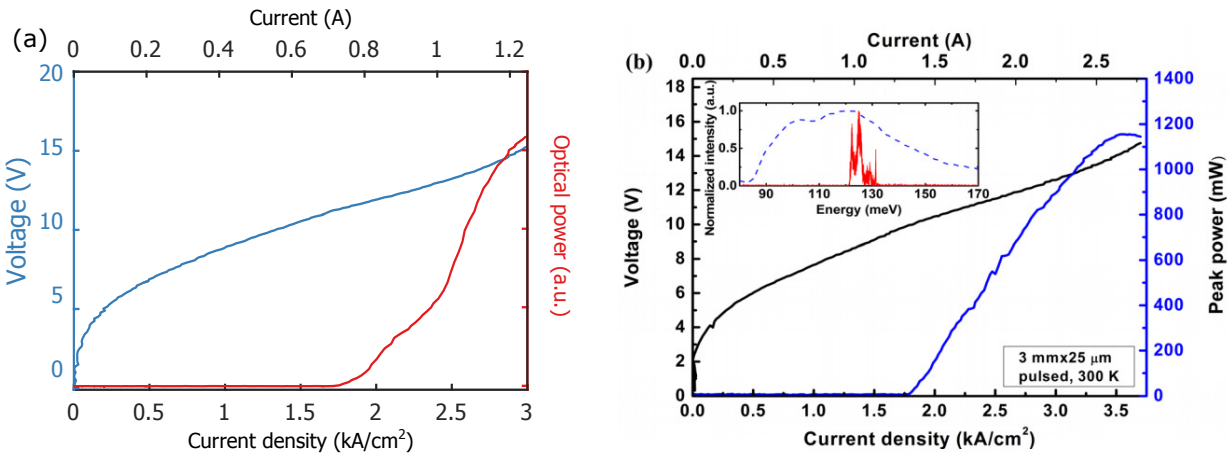

Figure 5.5: (a) Measured IVL curve of a wet etched epi-device, 15 μm wide 2 mm long. (b) Reported IVL curve in pulsed mode operation for a 25 μm wide 3 mm long FP laser. The inset shows the EL spectrum at threshold and the lasing spectrum at roll-over current density. [23]

second fully reflective mirror, causing phase change to different wavelength, leading to chromatic dispersion. The phase change and the dispersion change periodically with optical frequency. Two ways of implementing GTI mirror have been tested. First, we attach a small piece of gold to a PC controlled stage, carefully place it very close (~10 μm) to the rear facet. Then we measure the beatnote from the device in relation to different stage positions.

Fig. 5.7 shows the plots of the GTI position vs. beatnote bandwidth. The narrow bandwidth of the beatnote shows signs of a comb device, however, the gap in the spectrum of a device in the comb regime makes it undesirable for spectroscopy purposes. Fig. 5.7.c shows clear periodic behavior of the beatnote with change GTI mirror position. It demonstrates the effectiveness of the dispersion introduced by the mirror to help form a comb, which should be implemented on future devices.

Another way of introducing GTI mirror is by incorporating a MEMS comb drive [144]. As shown in Fig. 5.8, the MEMS comb drive has a plunger with mirror at the end, it is attached properly to the copper mount where the device is mounted. When voltage is applied, the plunger along with the mirror will move along the ridge direction (several microns), changing the dispersion introduced to the cavity. Fig. 5.9 shows how the beatnote changes with different biasing voltage on the MEMS

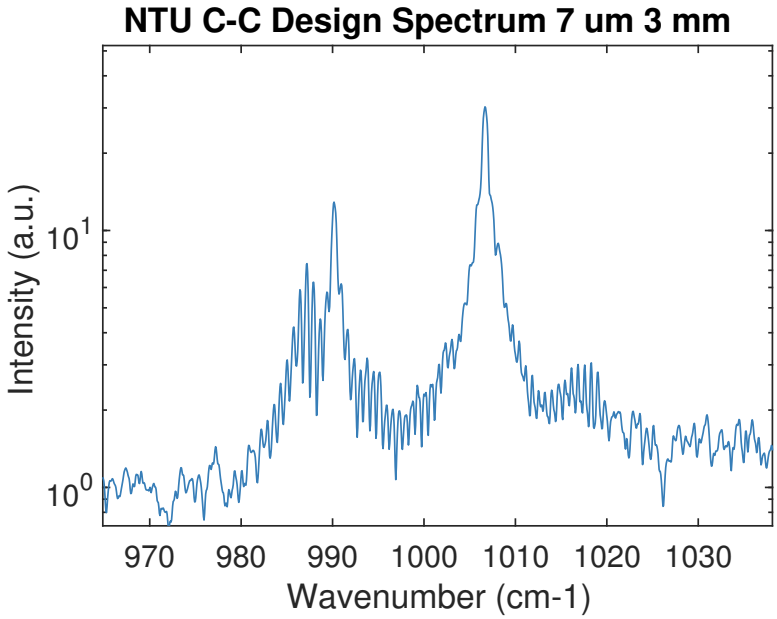

Figure 5.6: Spectrum of an NTU continuum-to-continuum design device, 7 um wide 3 mm long.

drive. The parabolic curve of the beatnote frequency shifting with applied voltage is in compatible with the displacement behavior of MEMS comb drives [145]. The comb regime is very sensitive to the mirro position (tens of nanometers), with very small bias change, the device can be easily tuned into and out of comb regime. This sensitive tunability, along with the fast modulation speed (kHz) of the MEMS comb drive, is very attractive for fast spectroscopy applications. The MEMS comb drive used in this setup is designed by Ningren Han [144] and fabricated by MEMSCAP.

5.4 MIT-Humboldt Device

Devices reported in this section is fabricated in the MIT cleanroom with MBE grown wafer from Prof. W. Ted Masselink's group in Humboldt University of Berlin. The dsign is a reported broadband gain medium lasing at $\sim$ 8.7 μm with a dual-upper-state to multiple-lower-state transition design [146]. The device is fabricated with wet etch epi-up process. The IVL characteristic of a 17 μm 2.87 mm device in pulse mode is shown in Fig. 5.10.

We implemented the movable GTI mirror on this device with a gold mirror at-

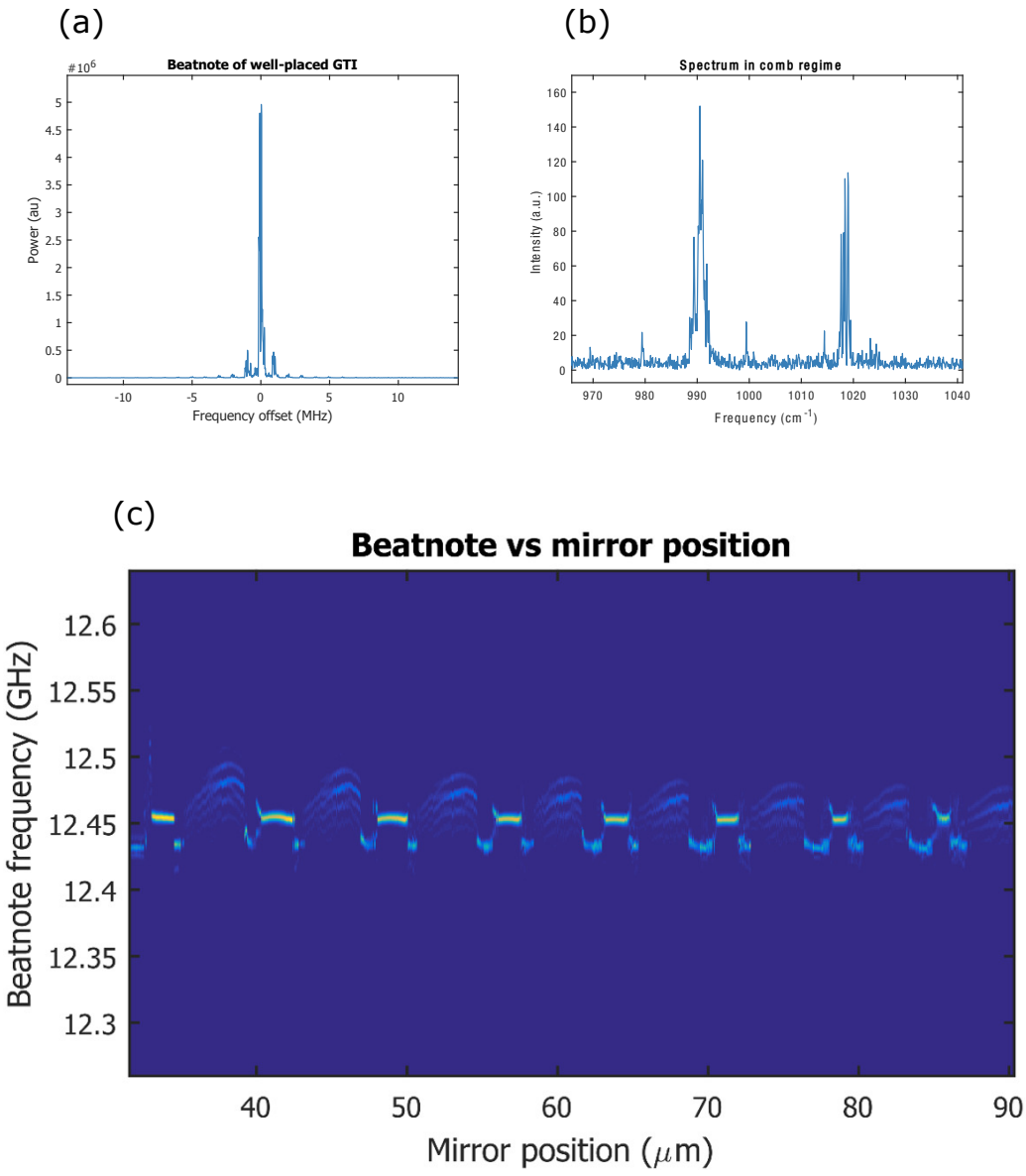

Figure 5.7: (a) Measured beatnote of a 15 um wide 3.5 mm long device centering at 12.46 GHz. (b) QCL spectrum in the comb regime with GTI mirror. (c) Plot of beatnote in relation to mirror position, showing clear periodic behavior.

(a)

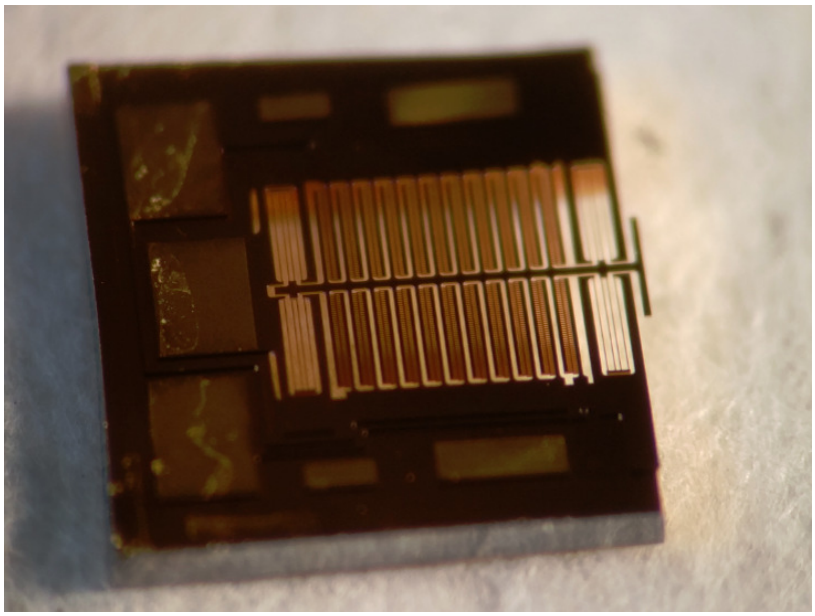

(b)

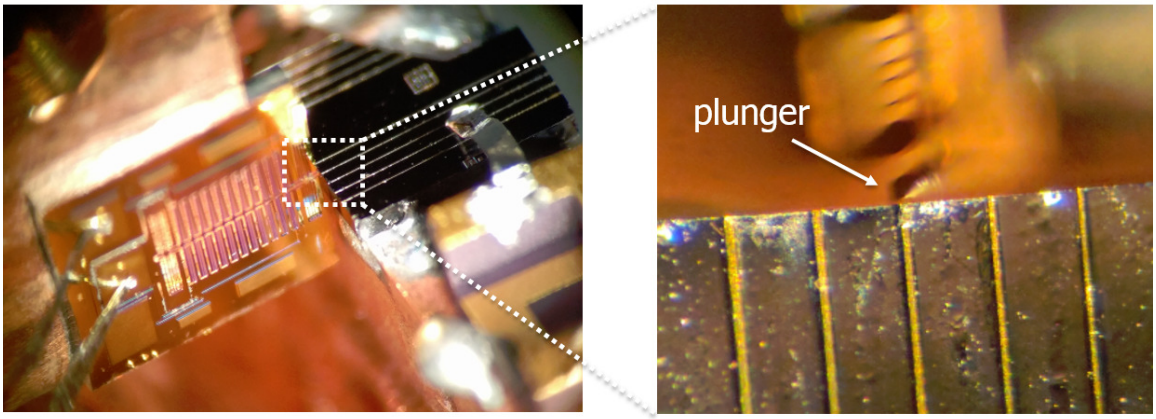

Figure 5.8: (a) An overview of the MEMS comb drive used as GTI movable mirror. (b) Closed up image of the relative position of the MEMS comb drive, laser ridge and the mirro attached to the plunger.

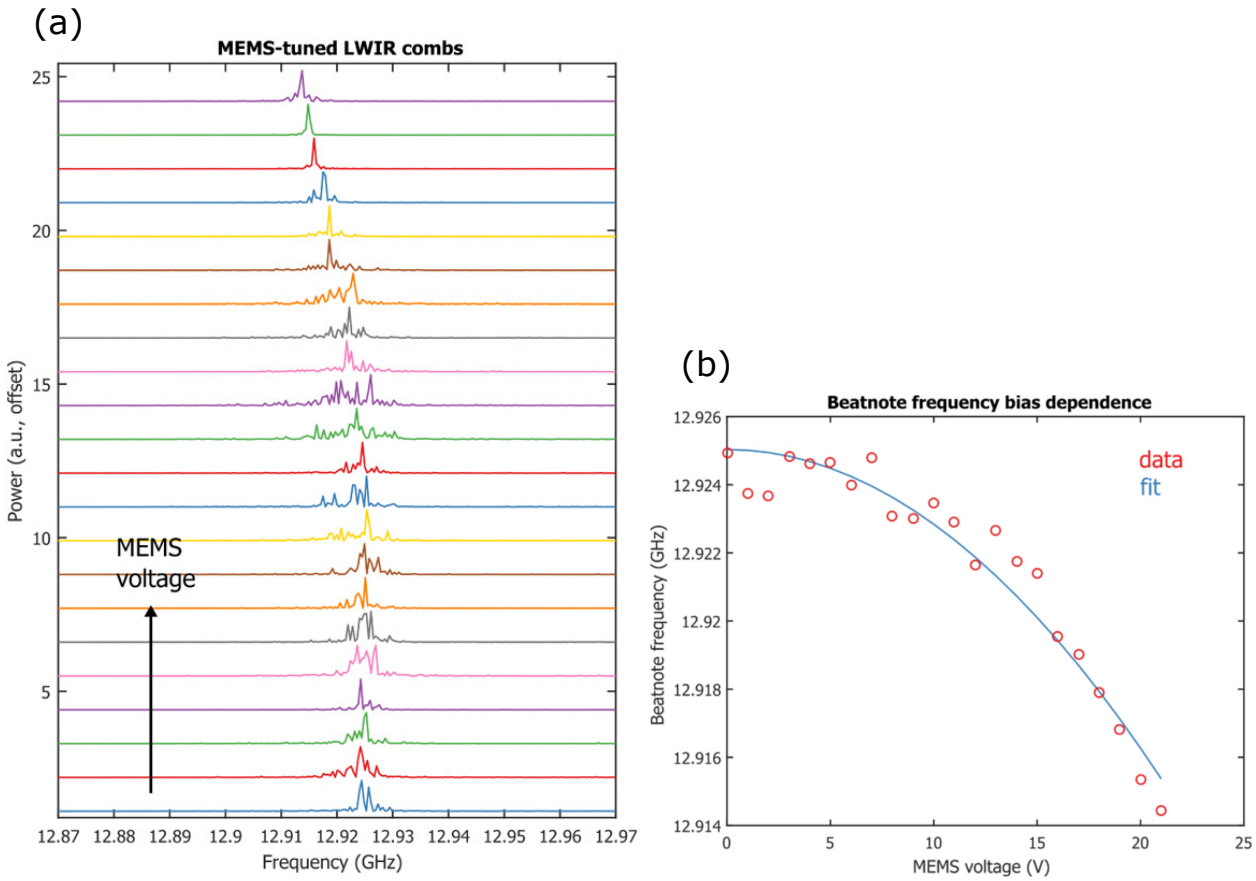

Figure 5.9: (a) Beatnote shift with MEMS comb drive changing in bias and position. (b) Plot of the beatnote frequency vs. MEMS bias. Shows the quadratic relationship, which is characteristic of MEMS comb drives. The fractional change of the beat note is 6e-4, which is about 1.8 μm for a 3 mm laser device. This value matches the characterization results for the MEMS comb drive.

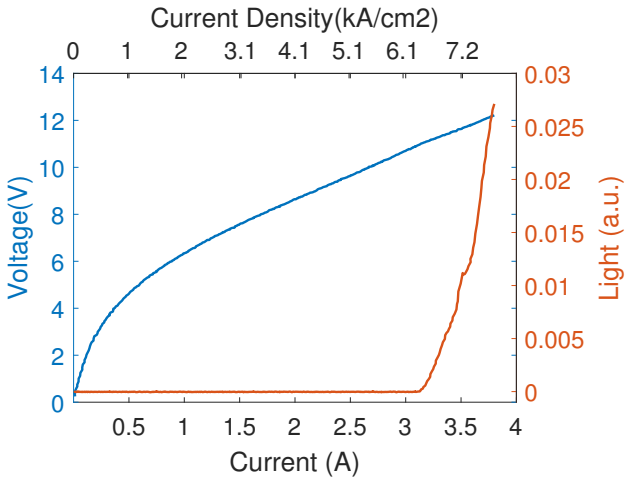

Figure 5.10: Current vs. voltage, current vs. light plot of a 17 um 2.87 mm device biased at 4 kHz 400 ns.

tached to a translation stage. In order to test the interaction between the GTI mirror and different lateral modes in the cavity, another stage is added allowing the mirror to move laterally (perpendicular to the laser ridge, in the same plane with the device). Essentially, when the mirror is moved laterally, only part of the facet will be covered, hence there will be a stronger interaction with higher order modes. FIg. 5.11 shows the comparison of the spectrum, inteferogram and beatnote with full and partial GTI mirror coverage.

The spectrum in comb-like regime has a bandwidth of $\sim$40 cm^{-1} with multiple peaks. The spectrum alone shows a clear sign of multimode lasing, with the comparison between the cases of full and partial mirror coverage further proving this point. According to Comsol mode simulation, when the ridge is narrow enough, higher order mode lasing will be surpressed. The beatnote is very broad (tens of MHz), which shows poor coherence between different modes. This can be improved by dispersion compensation and possibly CW operation.

The echo pulse from the device in FTIR is measured to obtain the GVD of the device, as discussed in the previous section. Fig. 5.12 shows the spectrum and interferogram of the 0th order peak and the 1st echo, along with the amplitude and phase of the echo measured at EL under different bias. Using the phase information

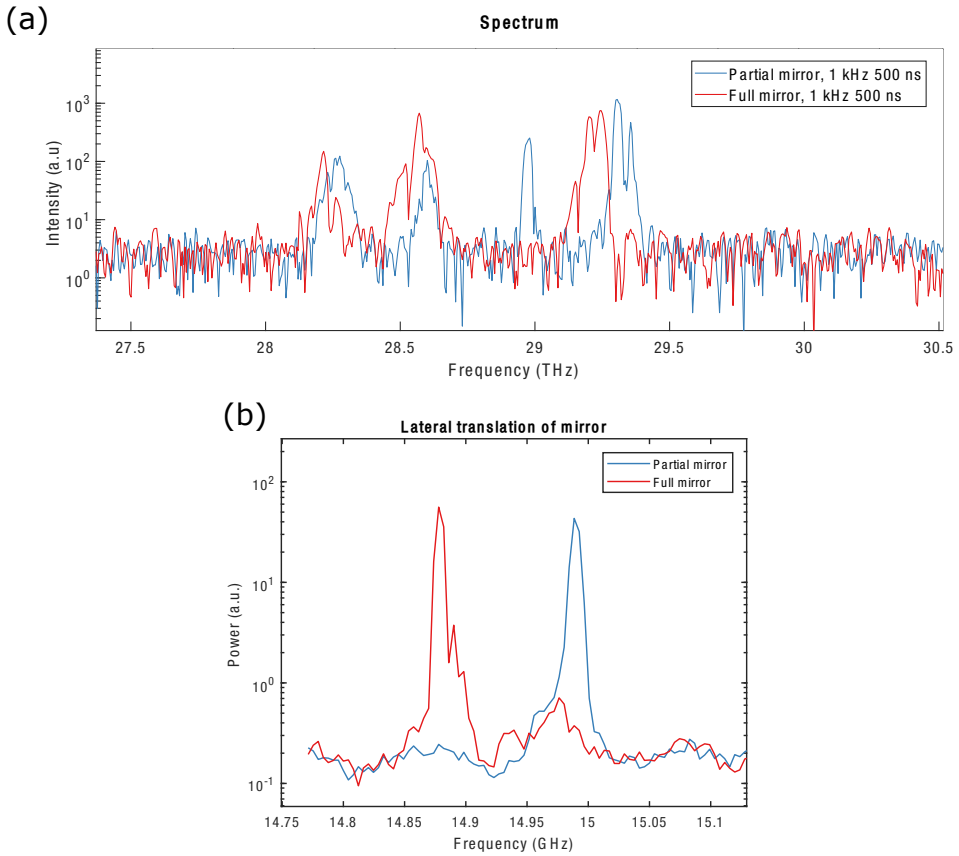

Figure 5.11: (a) Spectrum of a 17 um 2.87 mm device with full and partial GTI mirror coverage at optimum position to form a comb regime. (b) Beatnote shift when the GTI mirror is interacting with different modes.

of the echo, we can calculate the GVD = -2500 fs^2/mm, which is essentially a scaled (also inverted, see (5.5)) second order fitting of the curve. As shown in the plot, the GVD is calculated from phase information at different biases to adjust to the dispersion change with bias [147]. Using the position of the peak and first echo (Fig. 5.12.b), one can also calculate the group index in the device, which is essentially the ratio of the distance between two pulses and laser cavity length, which is n_{group}=(159.6 mm - 149.9 mm) / 2.87 mm = 3.38.

After the measurement of GVD, dispersion compensation structures can be designed. A big challenge for such a compensator for LWIR QCLs, as compared to THz [5], is the fact that it has a much smaller wavelength, which will make the dimension of the structure 10 times smaller, to sub micron level. This for sure pose a huge challenge for both simulation and fabrication. The simulation work is still ongoing,

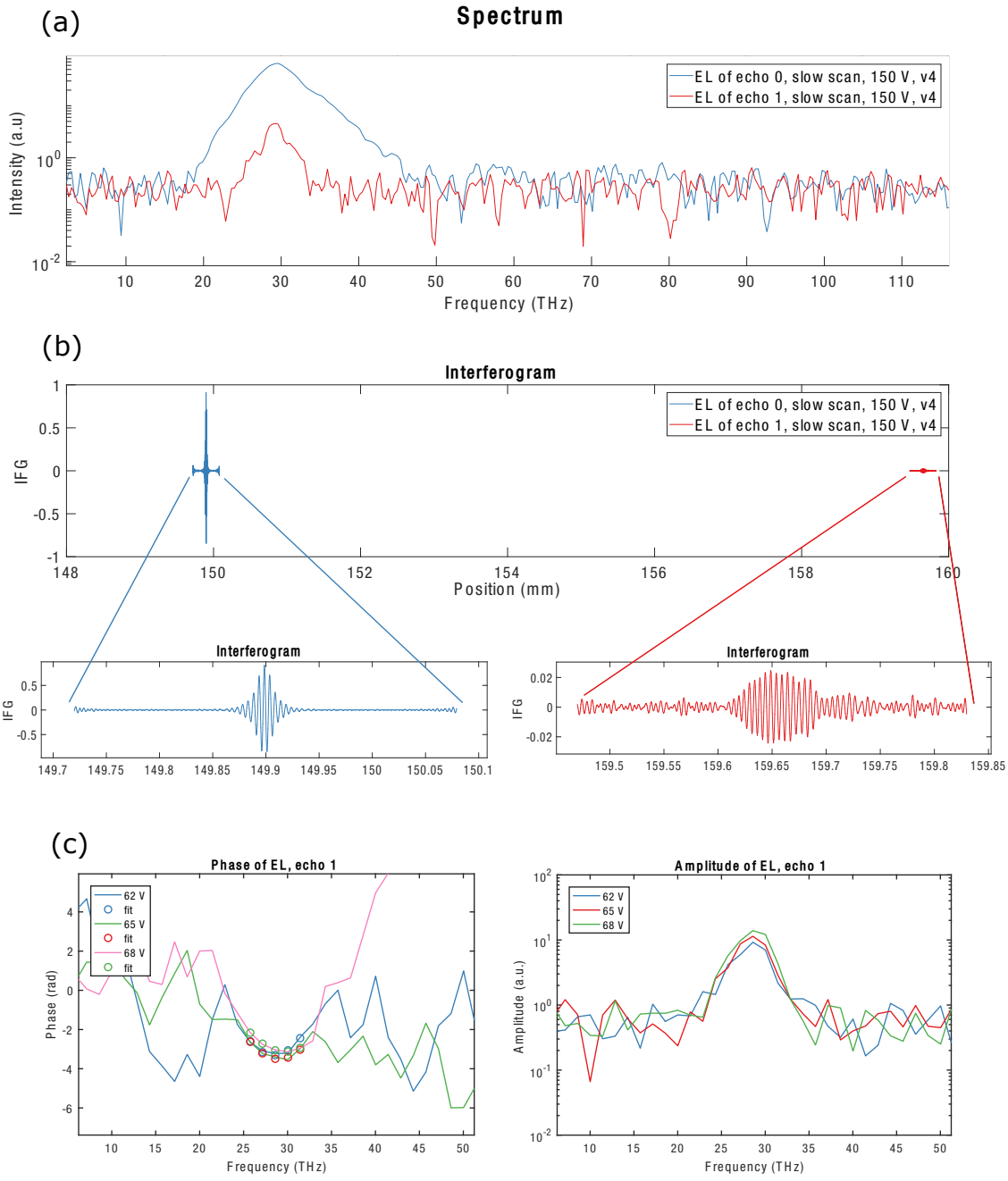

Figure 5.12: (a) Spectrum of the center peak and 1st order echo pulse. (b) Interferogram of two slow scans for center peak and 1st order echo pulse, showing their corresponding moving mirror position. Using this position, one can also calculate the group index in the device, which is essentially the ratio of the distance between two pulses and laser cavity length, which is n_{group}=(159.6 mm - 149.9 mm) / 2.87 mm = 3.38. (c) Amplitude and phase of the 1st EL echo under different bias. The fit of the phase gives a GVD of -2500 fs^2/mm.

and is based on a top grating approach, as shown in Fig. 5.13. The top grating will have chirped period and amplitude (etch depth or duty cycle of the grating). Since a negative GVD is measured, which means longer wavelength travels slower, to compensate for that, larger periods of gratings will be closer to the front facet, while shorter period will be at the end, to make longer-wavelength components travel shorter.

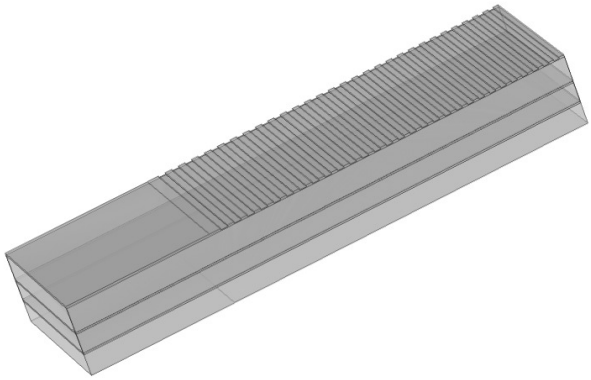

Figure 5.13: Comsol simulation strucure with chirped top grating on a FP laser ridge.

5.5 Conclusion and Future Work

In this thesis, the author has discussed the development history of QCL devices, theory and application of QCL frequency combs, LWIR QCL design and fabrication techniques. Established epi-up wet etch process is discussed in detail, along with preliminary results in dry etch recipe and epi-down fabrication. The characterization of 3 LWIR QCL devices are reported, 2 of which have shown a comb regime with GTI mirror. But further improvements will be needed for those two devices to be useful for spectroscopic applications.

The future work will be centered around the development of LWIR QCL frequency comb devices, which include the optimization of dry-etch recipe, the establishment of epi-down fabrication process for CW operation, the simulation and design of disper-

sion compensation structures, and the implementation of QWIP for beatnote measurement.

Appendix A

Detailed Fabrication Flow for Epi-Down Devices

Longwave Infrared Quantum Cascade Lasers with Double Alloy Contact

9 August 2017

Tianyi Zeng

MTL ID: tianyiz

Description: Extension of quantum cascade laser fabrication previously approved with top surface grating and electroplated gold

Facilities used: TRL, EML (Last Step)

Starting materials: InP wafers with MBE grown InGaAs/InAlAs heterostructures from Sandia National Laboratories.

Part 1. Surface Grating Definition

Step	Description	Lab	Machine	Comments
1.	Cleave and name MBE samples	TRL		Sample size ~1 x 1.5 cm. Gently scribe MBE wafer name onto one edge (for identifying crystal orientation and different designs).
2.	Positive resist coating	TRL	Coater	Use 3 solvent clean immediately before coating. SPR700 Dispense/Spread/Spin for 1/6/30s at 0.5/0.75/4.25 krpm. Follow with 30min prebake (95C). Note: Do HMDS if it is necessary.
3.	Photoresist exposure	TRL	MA-6	7s low vacuum exposure.
4.	Post-exposure bake	TRL	Hotplate	Set hotplate to 115 degC, place a (Si) dummy wafer on top of hotplate. Put sample on dummy, 1 min.
5.	Development	TRL	Photo-wet	MF-CD-26 90 s Follow by 30 min post-bake (120 C).
6.	Wet Etch	TRL	Acid-hood	Etch surface grating to a depth of 100 nm in H3PO4:HCl (1:1) (1 – 2.5 um/min)
7.	Photoresist removal	TRL	Photo-wet	Soak in clean acetone for ~30 mins to remove the photoresist, followed by methanol and IPA clean.

Part 2. Mesa Definition

Step	Description	Lab	Machine	Comments
8.	Predeposition oxide strip	TRL	Acid-hood	30s dip in 1:1 HCl: H2O, or 10s dip in BOE.

9.	Positive resist coating	TRL	Coater	Use 3 solvent clean immediately before coating. SPR700 Dispense/Spread/Spin for 1/6/30s at 0.5/0.75/4.25 krpm. Follow with 30min prebake (95C). Note: Do HMDS if it is necessary.
10.	Photoresist exposure	TRL	MA-6	7s low vacuum exposure.
11.	Post-exposure bake	TRL	Hotplate	Set hotplate to 115 degC, place a (Si) dummy wafer on top of hotplate. Put sample on dummy, 1 min.
12.	Development	TRL	Photo-wet	MF-CD-26 90 s Follow by 30 min post-bake (120 C).
13.	Wet etch	TRL	Acid-hood	Etch mesas in aged (20 min) HBr:HCL:H2O2:H2O (10:5:1:50)(~1um/min).

Part 3 Silicon Dioxide Definition

Step	Description	Lab	Machine	Comment
14.	Photoresist removal	TRL	Photo-wet	Soak in clean acetone for ~30 mins to remove the photoresist, followed by methanol and IPA clean.
15.	Dielectric layer deposition	TRL	STS-CVD	Deposit 4500 A high frequency SiO2 on top of the sample.
16.	Positive resist coating	TRL	Coater	Use 3 solvent clean immediately before coating. HMDS Primer. SPR Dispense/Spread/Spin for 1/6/30s at 0.5/0.75/4.25 krpm. Follow with 30min prebake (95C).
17.	Photoresist exposure	TRL	MA6	7s low vacuum exposure.
18.	Post-exposure bake	TRL	Hotplate	Set hotplate to 115 degC, place a (Si) dummy wafer on top of hotplate. Put sample on dummy, 1 min.
19.	Development	TRL	Photo-wet	MF-CD-26 40 s Follow by 30 min post-bake (120 C).
20.	Wet etch	TRL	Acid-hood	Dip samples in BOE. Rinse and agitate in water twice. Do not agitate the solution. 3-solvent cleaning. Acetone to get rid of the photoresist on the silicon dioxide. Asher for 15 min.

Part 4 Top Metal Definition

Step	Description	Lab	Machine	Comment
21.	Image reversal resist coating	TRL	Coater	Use 3 solvent clean immediately before coating. AZ5214E photoresist Dispense/Spread/Spin for 6/8/30s at 0.5/0.75/3.95 krpm Follow with 20min **prebake** (95 C).
22.	Photoresist exposure	TRL	MA-6	7s low vacuum exposure.
23.	Image reversal bake	TRL	hot-plate 1,2 or 3	120 C bake for 1 min. Bake on top of a silicon dummy, monitor temperature using contact thermometer.
24.	Flood exposure	TRL	MA-6	Flood expose all samples for 135s.
25.	Development	TRL	photo-wet	AZMIF422 for 2 min 30 sec. Follow by two rinses in DI water for 1 minute each.
26.	Postdevelopment clean	TRL	Asher	Ash for 5 min to remove possible photoresist residues.
27.	Top metal deposition	TRL	ebeamAu	Ta/Au 200A/1000A deposited at 1A/s.
28.	Lift-off	TRL		Soak all pieces for ~2 h in acetone. Clean samples in methanol and IPA afterwards.

Part 5 Backside Metallization and Electroplating Gold

Step	Description	Lab	Machine	Comment
29.	Backside metal deposition	TRL	ebeam Au/ ebeam FP	Deposit Ge/Au/Ni/Au (20 nm/ 50 nm/ 40 nm/ 50 nm)
30.	Annealing	ICL	RTA-pieces	RTA 400 C 30s, N2 atmosphere
31.	Electroplating	EML	2DTransfer Plating Hood	Electroplating Au 5 um

Bibliography

[1] M. Tonouchi, "Cutting-edge terahertz technology," *Nature photonics*, vol. 1, no. 2, pp. 97–105, 2007.

[2] A. Schliesser, N. Picqué, and T. W. Hänsch, "Mid-infrared frequency combs," *Nature Photonics*, vol. 6, no. 7, pp. 440–449, 2012.

[3] H. Telle, D. Meschede, and T. Hänsch, "Realization of a new concept for visible frequency division: phase locking of harmonic and sum frequencies," *Optics letters*, vol. 15, no. 10, pp. 532–534, 1990.

[4] T. J. Kippenberg, R. Holzwarth, and S. Diddams, "Microresonator-based optical frequency combs," *Science*, vol. 332, no. 6029, pp. 555–559, 2011.

[5] D. Burghoff, T.-Y. Kao, N. Han, C. W. I. Chan, X. Cai, Y. Yang, D. J. Hayton, J.-R. Gao, J. L. Reno, and Q. Hu, "Terahertz laser frequency combs," *Nature Photonics*, vol. 8, no. 6, pp. 462–467, 2014.

[6] A. Hugi, G. Villares, S. Blaser, H. Liu, and J. Faist, "Mid-infrared frequency comb based on a quantum cascade laser," *Nature*, vol. 492, no. 7428, p. 229, 2012.

[7] G. Villares, A. Hugi, S. Blaser, and J. Faist, "Dual-comb spectroscopy based on quantum-cascade-laser frequency combs," *Nature Communications*, vol. 5, p. 5192, 2014.

[8] Y. Yang, D. Burghoff, D. J. Hayton, J.-R. Gao, J. L. Reno, and Q. Hu, "Terahertz multiheterodyne spectroscopy using laser frequency combs," *Optica*, vol. 3, no. 5, pp. 499–502, 2016.

[9] Y. V. Flores, *Mid-infrared quantum cascade lasers: theoretical and experimental studieson temperature-driven scattering.* PhD thesis, Mathematisch-Naturwissenschaftliche Fakultät, 2015.

[10] C. Sirtori, C. Gmachl, F. Capasso, J. Faist, D. L. Sivco, A. L. Hutchinson, and A. Y. Cho, "Long-wavelength ($\lambda \sim$8–11.5 μm) semiconductor lasers with waveguides based on surface plasmons," *Optics letters*, vol. 23, no. 17, pp. 1366–1368, 1998.

[11] Y. Bidaux, I. Sergachev, W. Wuester, R. Maulini, T. Gresch, A. Bismuto, S. Blaser, A. Muller, and J. Faist, "Plasmon-enhanced waveguide for dispersion compensation in mid-infrared quantum cascade laser frequency combs," *Optics Letters*, vol. 42, no. 8, pp. 1604–1607, 2017.

[12] X. Huang, Y. Chiu, W. O. Charles, and C. Gmachl, "Ridge-width dependence of the threshold of long wavelength (λâĽĹ 14 μm) quantum cascade lasers with sloped and vertical sidewalls," *Optics express*, vol. 20, no. 3, pp. 2539–2547, 2012.

[13] B. Meng, *Tunable mid-infrared quantum cascade lasers*. PhD thesis, 2015.

[14] A. Evans, S. Darvish, S. Slivken, J. Nguyen, Y. Bai, and M. Razeghi, "Buried heterostructure quantum cascade lasers with high continuous-wave wall plug efficiency," *Applied Physics Letters*, vol. 91, no. 7, p. 071101, 2007.

[15] F. Yan, J. Zhang, C. Liu, N. Zhuo, F. Liu, S. Zhai, and Z. Wang, "Sample grating distributed feedback quantum cascade laser array," *Nanoscale research letters*, vol. 10, no. 1, p. 406, 2015.

[16] A. Wittmann, A. Hugi, E. Gini, N. Hoyler, and J. Faist, "Heterogeneous high-performance quantum-cascade laser sources for broad-band tuning," *IEEE Journal of Quantum Electronics*, vol. 44, no. 11, pp. 1083–1088, 2008.

[17] A. J. Evans, *GasMBE growth and characterization of strained layer InP-GaInAs-AlInAs quantum cascade lasers*. PhD thesis, NORTHWESTERN UNIVERSITY, 2008.

[18] Y. Yao, A. J. Hoffman, and C. F. Gmachl, "Mid-infrared quantum cascade lasers," *Nature Photonics*, vol. 6, no. 7, pp. 432–439, 2012.

[19] P. Fuchs, J. Friedl, S. Höfling, J. Koeth, A. Forchel, L. Worschech, and M. Kamp, "Single mode quantum cascade lasers with shallow-etched distributed bragg reflector," *Optics express*, vol. 20, no. 4, pp. 3890–3897, 2012.

[20] D. Hofstetter, J. Faist, M. Beck, A. Müller, and U. Oesterle, "Demonstration of high-performance 10.16 μm quantum cascade distributed feedback lasers fabricated without epitaxial regrowth," *Applied physics letters*, vol. 75, no. 5, pp. 665–667, 1999.

[21] R. Maulini, *Broadly tunable mid-infrared quantum cascade lasers for spectroscopic applications*. PhD thesis, Université de Neuchâtel, 2006.

[22] D. P. Burghoff, *Characterization of mid-infrared quantum cascade lasers*. PhD thesis, Massachusetts Institute of Technology, 2009.

[23] B. Meng, Y. Q. Zeng, G. Liang, J. Tao, X. N. Hu, E. Rodriguez, and Q. J. Wang, "Broadly continuously tunable slot waveguide quantum cascade lasers based on a continuum-to-continuum active region design," *Applied Physics Letters*, vol. 107, no. 11, p. 111110, 2015.

[24] J. Byrnes, *Unexploded ordnance detection and mitigation*. Springer Science & Business Media, 2008.

[25] J. Faist, F. Capasso, D. L. Sivco, C. Sirtori, A. L. Hutchinson, A. Y. Cho, *et al.*, "Quantum cascade laser," *Science*, vol. 264, no. 5158, pp. 553–556, 1994.

[26] R. P. Feynman, "There's plenty of room at the bottom," *Engineering and science*, vol. 23, no. 5, pp. 22–36, 1960.

[27] W. P. McCray, "Mbe deserves a place in the history books," *Nature nanotechnology*, vol. 2, no. 5, pp. 259–261, 2007.

[28] J. Arthur Jr, "Interaction of ga and as2 molecular beams with gaas surfaces," *Journal of Applied Physics*, vol. 39, no. 8, pp. 4032–4034, 1968.

[29] A. Y. Cho, "Epiaxial growth of gaas by molecular beam epitaxy," *J. Appl. Phys.*, vol. 41, p. 2780, 1970.

[30] K. G. Gunthner, "Three-temperature method," *Z. Naturforschg*, vol. 13a, p. 1081, 1958.

[31] L. Esaki and R. Tsu, "Superlattice and negative differential conductivity in semiconductors," *IBM Journal of Research and Development*, vol. 14, no. 1, pp. 61–65, 1970.

[32] S. R. Kazarinov R, "Possibility of the amplification of electromagnetic waves in a semiconductor with a superlattice," *Soviet Physics - Semiconductors*, vol. 5, no. 4, p. 707, 1971.

[33] J. Faist, C. Gmachl, F. Capasso, C. Sirtori, D. L. Sivco, J. N. Baillargeon, and A. Y. Cho, "Distributed feedback quantum cascade lasers," *Applied Physics Letters*, vol. 70, no. 20, pp. 2670–2672, 1997.

[34] M. Beck, D. Hofstetter, T. Aellen, J. Faist, U. Oesterle, M. Ilegems, E. Gini, and H. Melchior, "Continuous wave operation of a mid-infrared semiconductor laser at room temperature," *Science*, vol. 295, no. 5553, pp. 301–305, 2002.

[35] M. Razeghi, "High-performance inp-based mid-ir quantum cascade lasers," *IEEE journal of selected topics in Quantum Electronics*, vol. 15, no. 3, pp. 941–951, 2009.

[36] Wikipedia, *https://en.wikipedia.org/wiki/Infrared*, April 2017.

[37] HyperPhysics, *http://hyperphysics.phy-astr.gsu.edu/hbase/ems3.html*.

[38] Gigahertz-Optik, *http://light-measurement.com/wavelength-range/*, 2017.

[39] J. Faist, F. Capasso, D. L. Sivco, A. L. Hutchinson, S.-N. G. Chu, and A. Y. Cho, "Short wavelength (λ 3.4 μ m) quantum cascade laser based on strained compensated ingaas/alinas," *Applied Physics Letters*, vol. 72, no. 6, pp. 680–682, 1998.

[40] F.-Q. Liu, Y.-Z. Zhang, Q.-S. Zhang, D. Ding, B. Xu, Z.-G. Wang, D.-S. Jiang, and B.-Q. Sun, "High-performance strain-compensated ingaas/inalas quantum cascade lasers," *Semiconductor science and technology*, vol. 15, no. 12, p. L44, 2000.

[41] M. Semtsiv, M. Ziegler, S. Dressler, W. Masselink, N. Georgiev, T. Dekorsy, and M. Helm, "Above room temperature operation of short wavelength (λ= 3.8 μ m) strain-compensated in 0.73 ga 0.27 as–alas quantum-cascade lasers," *Applied physics letters*, vol. 85, no. 9, pp. 1478–1480, 2004.

[42] R. Teissier, D. Barate, A. Vicet, C. Alibert, A. Baranov, X. Marcadet, C. Renard, M. Garcia, C. Sirtori, D. Revin, *et al.*, "Room temperature operation of inas/ alsb quantum cascade lasers," *Applied physics letters*, vol. 85, no. 2, pp. 167–169, 2004.

[43] C. Gmachl, N. Owschimikow, A. Belyanin, A. Sergent, D. Sivco, M. Peabody, A. Cho, and F. Capasso, "Temperature dependence and single-mode tuning behavior of second-harmonic generation in quantum cascade lasers," *Applied physics letters*, vol. 84, no. 15, pp. 2751–2753, 2004.

[44] J. Yu, A. Evans, S. Slivken, S. Darvish, and M. Razeghi, "Short wavelength (/spl lambda//spl sim/4.3/spl mu/m) high-performance continuous-wave quantum-cascade lasers," *IEEE photonics technology letters*, vol. 17, no. 6, pp. 1154–1156, 2005.

[45] Q. Yang, C. Manz, W. Bronner, K. Köhler, and J. Wagner, "Room-temperature short-wavelength ($\lambda \sim$ 3.7–3.9 μ m) ga in as/ al as sb quantum-cascade lasers," *Applied physics letters*, vol. 88, no. 12, p. 121127, 2006.

[46] J. Devenson, D. Barate, O. Cathabard, R. Teissier, and A. Baranov, "Very short wavelength (λ= 3.1–3.3 μ m) quantum cascade lasers," *Applied physics letters*, vol. 89, no. 19, p. 191115, 2006.

[47] M. P. Semtsiv, M. Wienold, S. Dressler, and W. T. Masselink, "Short-wavelength ($\lambda \sim 3.3\,\mu$m) inp-based strain-compensated quantum-cascade laser," *Applied Physics Letters*, vol. 89, no. 21, p. 211124, 2006.

[48] J. S. Yu, S. R. Darvish, A. Evans, J. Nguyen, S. Slivken, and M. Razeghi, "Room-temperature continuous-wave operation of quantum-cascade lasers at λ = 4Îijm," *Applied Physics Letters*, vol. 88, no. 4, p. 041111, 2006.

[49] C. Sirtori, P. Kruck, S. Barbieri, H. Page, J. Nagle, M. Beck, J. Faist, and U. Oesterle, "Low-loss al-free waveguides for unipolar semiconductor lasers," *Applied Physics Letters*, vol. 75, no. 25, pp. 3911–3913, 1999.

[50] J. Devenson, O. Cathabard, R. Teissier, and A. Baranov, "High temperature operation of λâĽĹ 3.3 μ m quantum cascade lasers," *Applied Physics Letters*, vol. 91, no. 14, p. 141106, 2007.

[51] Y. Bai, S. Darvish, S. Slivken, W. Zhang, A. Evans, J. Nguyen, and M. Razeghi, "Room temperature continuous wave operation of quantum cascade lasers with watt-level optical power," *Applied Physics Letters*, vol. 92, no. 10, p. 101105, 2008.

[52] O. Cathabard, R. Teissier, J. Devenson, J. Moreno, and A. Baranov, "Quantum cascade lasers emitting near 2.6 μ m," *Applied Physics Letters*, vol. 96, no. 14, p. 141110, 2010.

[53] T. Kruczek, K. Fedorova, G. Sokolovskii, R. Teissier, A. Baranov, and E. Rafailov, "Inas/alsb widely tunable external cavity quantum cascade laser around 3.2 μm," *Applied Physics Letters*, vol. 102, no. 1, p. 011124, 2013.

[54] F. Capasso, J. Faist, C. Sirtori, and A. Cho, "Infrared (4–11 μm) quantum cascade lasers," *Solid State Communications*, vol. 102, no. 2-3, pp. 231–236, 1997.

[55] C. Gmachl, F. Capasso, A. Tredicucci, D. Sivco, A. Hutchinson, and A. Cho, "Long wavelength (/spl lambda//spl sime/13/spl mu/m) quantum cascade lasers," *Electronics Letters*, vol. 34, no. 11, pp. 1103–1104, 1998.

[56] J. Faist, F. Capasso, C. Sirtori, D. L. Sivco, J. N. Baillargeon, A. L. Hutchinson, S.-N. G. Chu, and A. Y. Cho, "High power mid-infrared (λ 5 μm) quantum cascade lasers operating above room temperature," *Applied Physics Letters*, vol. 68, no. 26, pp. 3680–3682, 1996.

[57] C. Sirtori, J. Faist, F. Capasso, D. Sivco, A. Hutchinson, and A. Cho, "Long wavelength infrared (λâĽĆ 11 μm) quantum cascade lasers," *Applied physics letters*, vol. 69, no. 19, pp. 2810–2812, 1996.

[58] G. Luo, C. Peng, H. Le, S. Pei, W.-Y. Hwang, B. Ishaug, J. Um, J. N. Baillargeon, and C.-H. Lin, "Grating-tuned external-cavity quantum-cascade semiconductor lasers," *Applied Physics Letters*, vol. 78, no. 19, pp. 2834–2836, 2001.

[59] C. Gmachl, D. L. Sivco, R. Colombelli, F. Capasso, and A. Y. Cho, "Ultra-broadband semiconductor laser," *Nature*, vol. 415, no. 6874, pp. 883–887, 2002.

[60] R. Maulini, A. Mohan, M. Giovannini, J. Faist, and E. Gini, "External cavity quantum-cascade laser tunable from 8.2 to 10.4 μ m using a gain element with a heterogeneous cascade," *Applied physics letters*, vol. 88, no. 20, p. 201113, 2006.

[61] A. Wittmann, A. Hugi, E. Gini, N. Hoyler, and J. Faist, "Heterogeneous high-performance quantum-cascade laser sources for broad-band tuning," *IEEE Journal of Quantum Electronics*, vol. 44, no. 11, pp. 1083–1088, 2008.

[62] A. Hugi, R. Terazzi, Y. Bonetti, A. Wittmann, M. Fischer, M. Beck, J. Faist, and E. Gini, "External cavity quantum cascade laser tunable from 7.6 to 11.4 μ m," *Applied Physics Letters*, vol. 95, no. 6, p. 061103, 2009.

[63] M. Razeghi, S. Slivken, Y. Bai, B. Gokden, and S. R. Darvish, "High power quantum cascade lasers," *New Journal of Physics*, vol. 11, no. 12, p. 125017, 2009.

[64] A. Hugi, A.-M. Lyon, M. Mangold, M. Geiser, W. Wüster, F. Kapsalidis, J. Pierre, and J. Faist, "Mid-infrared spectrometer featuring μ-second time resolution based on dual-comb quantum cascade laser frequency combs," in *CLEO: Applications and Technology*, pp. AF1B–1, Optical Society of America, 2017.

[65] A. Evans, J. Yu, S. Slivken, and M. Razeghi, "Continuous-wave operation of λ 4.8 μ m quantum-cascade lasersat room temperature," *Applied Physics Letters*, vol. 85, no. 12, pp. 2166–2168, 2004.

[66] Y. Bai, N. Bandyopadhyay, S. Tsao, S. Slivken, and M. Razeghi, "Room temperature quantum cascade lasers with 27% wall plug efficiency," *Applied Physics Letters*, vol. 98, no. 18, p. 181102, 2011.

[67] Y. Bai, S. Darvish, S. Slivken, W. Zhang, A. Evans, J. Nguyen, and M. Razeghi, "Room temperature continuous wave operation of quantum cascade lasers with watt-level optical power," *Applied Physics Letters*, vol. 92, no. 10, p. 101105, 2008.

[68] Q. Lu, Y. Bai, N. Bandyopadhyay, S. Slivken, and M. Razeghi, "Room-temperature continuous wave operation of distributed feedback quantum cascade lasers with watt-level power output," *Applied Physics Letters*, vol. 97, no. 23, p. 231119, 2010.

[69] M. Nobile, P. Klang, E. Mujagic, H. Detz, A. Andrews, W. Schrenk, and G. Strasser, "Quantum cascade laser utilising aluminium-free material system: Ingaas/gaassb lattice-matched to inp," *Electronics letters*, vol. 45, no. 20, pp. 1031–1033, 2009.

[70] E. Pickwell and V. Wallace, "Biomedical applications of terahertz technology," *Journal of Physics D: Applied Physics*, vol. 39, no. 17, p. R301, 2006.

[71] A. W. M. Lee, T.-Y. Kao, D. Burghoff, Q. Hu, and J. L. Reno, "Terahertz tomography using quantum-cascade lasers," *Optics letters*, vol. 37, no. 2, pp. 217–219, 2012.

[72] I. F. Akyildiz, J. M. Jornet, and C. Han, "Terahertz band: Next frontier for wireless communications," *Physical Communication*, vol. 12, pp. 16–32, 2014.

[73] D. P. Burghoff, *Broadband terahertz photonics*. PhD thesis, Massachusetts Institute of Technology, 2014.

[74] M. Helm, E. Colas, P. England, F. DeRosa, and S. Allen Jr, "Observation of grating-induced intersubband emission from gaas/algaas superlattices," *Applied physics letters*, vol. 53, no. 18, pp. 1714–1716, 1988.

[75] R. Köhler, A. Tredicucci, F. Beltram, H. E. Beere, E. H. Linfield, A. G. Davies, D. A. Ritchie, R. C. Iotti, and F. Rossi, "Terahertz semiconductor-heterostructure laser," *Nature*, vol. 417, no. 6885, pp. 156–159, 2002.

[76] G. Scalari, L. Ajili, J. Faist, H. Beere, E. Linfield, D. Ritchie, and G. Davies, "Far-infrared (λâĽČ 87 μ m) bound-to-continuum quantum-cascade lasers operating up to 90 k," *Applied Physics Letters*, vol. 82, no. 19, pp. 3165–3167, 2003.

[77] J. Faist, M. Beck, T. Aellen, and E. Gini, "Quantum-cascade lasers based on a bound-to-continuum transition," *Applied Physics Letters*, vol. 78, no. 2, pp. 147–149, 2001.

[78] B. S. Williams, H. Callebaut, S. Kumar, Q. Hu, and J. L. Reno, "3.4-thz quantum cascade laser based on longitudinal-optical-phonon scattering for depopulation," *Applied Physics Letters*, vol. 82, no. 7, pp. 1015–1017, 2003.

[79] S. Kumar, Q. Hu, and J. L. Reno, "186 k operation of terahertz quantum-cascade lasers based on a diagonal design," *Applied Physics Letters*, vol. 94, no. 13, p. 131105, 2009.

[80] S. Fathololoumi, E. Dupont, C. Chan, Z. Wasilewski, S. Laframboise, D. Ban, A. Mátyás, C. Jirauschek, Q. Hu, and H. Liu, "Terahertz quantum cascade lasers operating up to 200 k with optimized oscillator strength and improved injection tunneling," *Optics express*, vol. 20, no. 4, pp. 3866–3876, 2012.

[81] S. Kumar, Q. Qin, B. S. Williams, Q. Hu, Z. R. Wasilewski, and H. Liu, "Quantum-cascade lasers with one-well injector operating at 1.59 thz (λ= 188.5 μm)," in *Conference on Lasers and Electro-Optics*, p. CWP1, Optical Society of America, 2007.

[82] G. Scalari, C. Walther, J. Faist, H. Beere, and D. Ritchie, "Electrically switchable, two-color quantum cascade laser emitting at 1.39 and 2.3 thz," *Applied physics letters*, vol. 88, no. 14, p. 141102, 2006.

[83] B. S. Williams, S. Kumar, Q. Hu, and J. L. Reno, "Operation of terahertz quantum-cascade lasers at 164 k in pulsed mode and at 117 k in continuous-wave mode," *Optics Express*, vol. 13, no. 9, pp. 3331–3339, 2005.

[84] B. S. Williams, S. Kumar, Q. Hu, and J. L. Reno, "High-power terahertz quantum-cascade lasers," *Electronics letters*, vol. 42, no. 2, pp. 89–91, 2006.

[85] L. Li, L. Chen, J. Zhu, J. Freeman, P. Dean, A. Valavanis, A. Davies, and E. Linfield, "Terahertz quantum cascade lasers with$>$ 1 w output powers," *Electronics Letters*, vol. 50, no. 4, pp. 309–311, 2014.

[86] L. Li, L. Chen, J. Freeman, M. Salih, P. Dean, A. Davies, and E. Linfield, "Multi-watt high-power thz frequency quantum cascade lasers," *Electronics Letters*, vol. 53, no. 12, pp. 799–800, 2017.

[87] K. Vijayraghavan, Y. Jiang, M. Jang, A. Jiang, K. Choutagunta, A. Vizbaras, F. Demmerle, G. Boehm, M. C. Amann, and M. A. Belkin, "Broadly tunable terahertz generation in mid-infrared quantum cascade lasers," *Nature communications*, vol. 4, p. 2021, 2013.

[88] Y. Yang, D. Burghoff, J. Reno, and Q. Hu, "Towards thz dual-comb spectrometer based on quantum cascade laser frequency combs," in *International Conference on Intersubband Transitions in Quantum Wells, Vienna, Austria (September 6–11, 2015)*, 2015.

[89] T. Udem, J. Reichert, R. Holzwarth, and T. Hänsch, "Accurate measurement of large optical frequency differences with a mode-locked laser," *Optics letters*, vol. 24, no. 13, pp. 881–883, 1999.

[90] T. Udem, J. Reichert, R. Holzwarth, and T. Hänsch, "Absolute optical frequency measurement of the cesium d 1 line with a mode-locked laser," *Physical review letters*, vol. 82, no. 18, p. 3568, 1999.

[91] T. Udem, A. Huber, B. Gross, J. Reichert, M. Prevedelli, M. Weitz, and T. W. Hänsch, "Phase-coherent measurement of the hydrogen 1 s- 2 s transition frequency with an optical frequency interval divider chain," *Physical Review Letters*, vol. 79, no. 14, p. 2646, 1997.

[92] C. Erny, K. Moutzouris, J. Biegert, D. Kühlke, F. Adler, A. Leitenstorfer, and U. Keller, "Mid-infrared difference-frequency generation of ultrashort pulses tunable between 3.2 and 4.8 μm from a compact fiber source," *Optics letters*, vol. 32, no. 9, pp. 1138–1140, 2007.

[93] P. Del Haye, A. Schliesser, O. Arcizet, T. Wilkins, R. Holzwarth, and T. Kippenberg, "Optical frequency comb generation from a monolithic microresonator," *arXiv preprint arXiv:0708.0611*, 2007.

[94] J. Riemensberger, K. Hartinger, T. Herr, V. Brasch, R. Holzwarth, and T. J. Kippenberg, "Dispersion engineering of thick high-q silicon nitride ring-resonators via atomic layer deposition," *Optics express*, vol. 20, no. 25, pp. 27661–27669, 2012.

[95] A. R. Johnson, Y. Okawachi, M. R. Lamont, J. S. Levy, M. Lipson, and A. L. Gaeta, "Microresonator-based comb generation without an external laser source," *Optics express*, vol. 22, no. 2, pp. 1394–1401, 2014.

[96] D. Burghoff, Y. Yang, and Q. Hu, "Computational multiheterodyne spectroscopy," *Science advances*, vol. 2, no. 11, p. e1601227, 2016.

[97] J. Khurgin, Y. Dikmelik, A. Hugi, and J. Faist, "Coherent frequency combs produced by self frequency modulation in quantum cascade lasers," *Applied Physics Letters*, vol. 104, no. 8, p. 081118, 2014.

[98] F. Keilmann, C. Gohle, and R. Holzwarth, "Time-domain mid-infrared frequency-comb spectrometer," *Optics letters*, vol. 29, no. 13, pp. 1542–1544, 2004.

[99] I. Coddington, N. Newbury, and W. Swann, "Dual-comb spectroscopy," *Optica*, vol. 3, no. 4, pp. 414–426, 2016.

[100] Y. Wang, M. G. Soskind, W. Wang, and G. Wysocki, "High-resolution multi-heterodyne spectroscopy based on fabry-perot quantum cascade lasers," *Applied Physics Letters*, vol. 104, no. 3, p. 031114, 2014.

[101] J. Westberg, L. Sterczewski, and G. Wysocki, "Mid-infrared multiheterodyne spectroscopy with phase-locked quantum cascade lasers," *Applied Physics Letters*, vol. 110, no. 14, p. 141108, 2017.

[102] J. Faist, *Quantum cascade lasers*. OUP Oxford, 2013.

[103] M. S. Vitiello, G. Scalari, B. Williams, and P. De Natale, "Quantum cascade lasers: 20 years of challenges," *Optics express*, vol. 23, no. 4, pp. 5167–5182, 2015.

[104] K. Fujita, "Mid-infrared ingaas/inalas quantum cascade lasers," 2014.

[105] G. F. F. Villares, *Quantum cascade laser frequency combs for spectroscopy applications*. PhD thesis, 2016.

[106] Y. Yao, W. O. Charles, T. Tsai, J. Chen, G. Wysocki, and C. F. Gmachl, "Broadband quantum cascade laser gain medium based on a "continuum-to-bound" active region design," *Applied Physics Letters*, vol. 96, no. 21, p. 211106, 2010.

[107] A. Tredicucci, F. Capasso, C. Gmachl, D. Sivco, A. Hutchinson, and A. Cho, "Long wavelength quantum cascade lasers," in *Nanostructures and Quantum Dots/WDM Components/VCSELs and Microcavaties/RF Photonics for CATV and HFC Systems, 1999 Digest of the LEOS Summer Topical Meetings*, pp. III43–III44, IEEE, 1999.

[108] C. Sirtori, F. Capasso, J. Faist, and S. Scandolo, "Nonparabolicity and a sum rule associated with bound-to-bound and bound-to-continuum intersubband transitions in quantum wells," *Physical Review B*, vol. 50, no. 12, p. 8663, 1994.

[109] J. Faist, C. Sirtori, F. Capasso, D. L. Sivco, J. N. Baillargeon, A. L. Hutchinson, and A. Y. Cho, "High-power long-wavelength ($\lambda \sim 11.5$ μm) quantum cascade lasers operating above room temperature," *IEEE Photonics Technology Letters*, vol. 10, no. 8, pp. 1100–1102, 1998.

[110] M. Rochat, L. Ajili, H. Willenberg, J. Faist, H. Beere, G. Davies, E. Linfield, and D. Ritchie, "Low-threshold terahertz quantum-cascade lasers," *Applied Physics Letters*, vol. 81, no. 8, pp. 1381–1383, 2002.

[111] B. S. Williams, S. Kumar, H. Callebaut, Q. Hu, and J. L. Reno, "Terahertz quantum-cascade laser at λâĽĹ 100 μ m using metal waveguide for mode confinement," *Applied Physics Letters*, vol. 83, no. 11, pp. 2124–2126, 2003.

[112] C. Sirtori, J. Faist, F. Capasso, D. L. Sivco, A. L. Hutchinson, and A. Y. Cho, "Quantum cascade laser with plasmon-enhanced waveguide operating at 8.4 μm wavelength," *Applied physics letters*, vol. 66, no. 24, pp. 3242–3244, 1995.

[113] Y. Flores, M. Elagin, S. Kurlov, A. Aleksandrova, G. Monastyrskyi, J. Kischkat, M. Semtsiv, and W. Masselink, "Growth initiation for buried-heterostructure quantum-cascade laser regrowth by gas-source molecular-beam epitaxy," *Journal of Crystal Growth*, vol. 398, pp. 40–44, 2014.

[114] J. Yu, S. Slivken, S. Darvish, A. Evans, B. Gokden, and M. Razeghi, "High-power, room-temperature, and continuous-wave operation of distributed-feedback quantum-cascade lasers at λ 4.8 μ m," *Applied physics letters*, vol. 87, no. 4, p. 041104, 2005.

[115] K. Fujita, S. Furuta, A. Sugiyama, T. Ochiai, A. Ito, T. Dougakiuchi, T. Edamura, and M. Yamanishi, "High-performance quantum cascade lasers with wide electroluminescence (600 cm- 1), operating in continuous-wave above 100Âř c," *Applied physics letters*, vol. 98, no. 23, p. 231102, 2011.

[116] T. J. Slight, G. Tandoi, D. G. Revin, A. McKee, S. Y. Zhang, W. Meredith, J. W. Cockburn, and C. N. Ironside, "λ˜ 3.35 m distributed-feedback quantum-cascade lasers with high-aspect-ratio lateral grating," *IEEE Photonics Technology Letters*, vol. 23, no. 5, p. 420, 2011.

[117] R. Maulini, A. Mohan, M. Giovannini, J. Faist, and E. Gini, "External cavity quantum-cascade laser tunable from 8.2 to 10.4 μ m using a gain element with a heterogeneous cascade," *Applied physics letters*, vol. 88, no. 20, p. 201113, 2006.

[118] M. G. Littman and H. J. Metcalf, "Spectrally narrow pulsed dye laser without beam expander," *Applied optics*, vol. 17, no. 14, pp. 2224–2227, 1978.

[119] A. Mohan, A. Wittmann, A. Hugi, S. Blaser, M. Giovannini, and J. Faist, "Room-temperature continuous-wave operation of an external-cavity quantum cascade laser," *Optics letters*, vol. 32, no. 19, pp. 2792–2794, 2007.

[120] P. Q. Liu, X. Wang, and C. F. Gmachl, "Single-mode quantum cascade lasers employing asymmetric mach-zehnder interferometer type cavities," *Applied Physics Letters*, vol. 101, no. 16, p. 161115, 2012.

[121] T. S. Mansuripur, S. Menzel, R. Blanchard, L. Diehl, C. Pflügl, Y. Huang, J.-H. Ryou, R. D. Dupuis, M. Loncar, and F. Capasso, "Widely tunable mid-infrared quantum cascade lasers using sampled grating reflectors," *Optics express*, vol. 20, no. 21, pp. 23339–23348, 2012.

[122] B. Meng, J. Tao, X. Hui Li, Y. Quan Zeng, S. Wu, and Q. Jie Wang, "Tunable single-mode slot waveguide quantum cascade lasers," *Applied Physics Letters*, vol. 104, no. 20, p. 201106, 2014.

[123] Q. Lu, D. Wu, S. Sengupta, S. Slivken, and M. Razeghi, "Room temperature continuous wave, monolithic tunable thz sources based on highly efficient mid-infrared quantum cascade lasers," *Scientific reports*, vol. 6, p. 23595, 2016.

[124] D. Hofstetter, M. Beck, T. Aellen, and J. Faist, "High-temperature operation of distributed feedback quantum-cascade lasers at 5.3 μm," *Applied Physics Letters*, vol. 78, no. 4, pp. 396–398, 2001.

[125] F. Fiedler, A. Schlachetzki, and G. Klein, "Material-selective etching of inp and an ingaasp alloy," *Journal of Materials Science*, vol. 17, no. 10, pp. 2911–2918, 1982.

[126] S. R. Bahl, W. Azzam, and J. del Alamo, "Strained-insulator in/sub x/al/sub 1-x/as/n/sup+/-in/sub 0.53/ga/sub 0.47/as heterostructure field-effect transistors," *IEEE Transactions on Electron Devices*, vol. 38, no. 9, pp. 1986–1992, 1991.

[127] M. Razeghi and S. Slivken, "High power quantum cascade lasers grown by gasmbe," *OPTOELECTRONICS REVIEW*, no. 2, pp. 85–92, 2003.

[128] S. B. Slivken, *Quantum cascade lasers grown by gas-source molecular beam epitaxy*. PhD thesis, Northwestern University, 2002.

[129] D. R. Greenberg, *The physics and technology of the InAlAs-InP heterostructure field-effect transistor*. PhD thesis, Massachusetts Institute of Technology, 1995.

[130] R. Bhat, J. Hayes, H. Schumacher, M. Koza, D. Hwang, and M. Meynadier, "High gain inp/ingaas heterojunction bipolar transistors grown by omcvd," *Journal of Crystal Growth*, vol. 93, no. 1-4, pp. 919–923, 1988.

[131] A. Stano, "Chemical etching characteristics of ingaas/inp and inalas/inp heterostructures," *Journal of the Electrochemical Society*, vol. 134, no. 2, pp. 448–452, 1987.

[132] G. C. DeSalvo, W. F. Tseng, and J. Comas, "Etch rates and selectivities of citric acid/hydrogen peroxide on gaas, al0. 3ga0. 7as, in0. 2ga0. 8as, in0. 53ga0. 47as, in0. 52al0. 48as, and inp," *Journal of The Electrochemical Society*, vol. 139, no. 3, pp. 831–835, 1992.

[133] Y. He, B. Liang, N. Tien, and C. Tu, "Selective chemical etching of inp over inalas," *Journal of The Electrochemical Society*, vol. 139, no. 7, pp. 2046–2048, 1992.

[134] J. S. Parker, E. J. Norberg, R. S. Guzzon, S. C. Nicholes, and L. A. Coldren, "High verticality inp/ingaasp etching in cl 2/h 2/ar inductively coupled plasma for photonic integrated circuits," *Journal of Vacuum Science & Technology B, Nanotechnology and Microelectronics: Materials, Processing, Measurement, and Phenomena*, vol. 29, no. 1, p. 011016, 2011.

[135] X. Zhao, J. Lin, C. Heidelberger, E. A. Fitzgerald, and J. A. del Alamo, "Vertical nanowire ingaas mosfets fabricated by a top-down approach," in *Electron Devices Meeting (IEDM), 2013 IEEE International*, pp. 28–4, IEEE, 2013.

[136] X. Zhao and J. A. del Alamo, "Nanometer-scale vertical-sidewall reactive ion etching of ingaas for 3-d iii-v mosfets," *IEEE Electron Device Letters*, vol. 35, no. 5, pp. 521–523, 2014.

[137] D. Burghoff, Y. Yang, D. J. Hayton, J.-R. Gao, J. L. Reno, and Q. Hu, "Evaluating the coherence and time-domain profile of quantum cascade laser frequency combs," *Optics express*, vol. 23, no. 2, pp. 1190–1202, 2015.

[138] H. Schneider and H. C. Liu, *Quantum well infrared photodetectors*. Springer, 2007.

[139] D. Burghoff, T.-Y. Kao, D. Ban, A. W. M. Lee, Q. Hu, and J. Reno, "A terahertz pulse emitter monolithically integrated with a quantum cascade laser," *Applied Physics Letters*, vol. 98, no. 6, p. 061112, 2011.

[140] D. Burghoff, C. Wang Ivan Chan, Q. Hu, and J. L. Reno, "Gain measurements of scattering-assisted terahertz quantum cascade lasers," *Applied Physics Letters*, vol. 100, no. 26, p. 261111, 2012.

[141] P. Tzenov, D. Burghoff, Q. Hu, and C. Jirauschek, "Time domain modeling of terahertz quantum cascade lasers for frequency comb generation," *Optics express*, vol. 24, no. 20, pp. 23232–23247, 2016.

[142] T. Dougakiuchi, K. Fujita, N. Akikusa, A. Sugiyama, T. Edamura, and M. Yamanishi, "Broadband tuning of external cavity dual-upper-state quantum-cascade lasers in continuous wave operation," *Applied physics express*, vol. 4, no. 10, p. 102101, 2011.

[143] K. Fujita, S. Furuta, A. Sugiyama, T. Ochiai, A. Ito, T. Dougakiuchi, T. Edamura, and M. Yamanishi, "High-performance quantum cascade lasers with wide electroluminescence (600 cm- 1), operating in continuous-wave above 100Âř c," *Applied physics letters*, vol. 98, no. 23, p. 231102, 2011.

[144] N. Han, A. de Geofroy, D. P. Burghoff, C. W. I. Chan, A. W. M. Lee, J. L. Reno, and Q. Hu, "Broadband all-electronically tunable mems terahertz quantum cascade lasers," *Optics letters*, vol. 39, no. 12, pp. 3480–3483, 2014.

[145] R. Legtenberg, A. Groeneveld, and M. Elwenspoek, "Comb-drive actuators for large displacements," *Journal of Micromechanics and microengineering*, vol. 6, no. 3, p. 320, 1996.

[146] K. Fujita, S. Furuta, T. Dougakiuchi, A. Sugiyama, T. Edamura, and M. Yamanishi, "Broad-gain ($\delta\lambda/\lambda$ 0˜ 0.4), temperature-insensitive (t 0˜ 510k) quantum cascade lasers," *Optics express*, vol. 19, no. 3, pp. 2694–2701, 2011.

[147] D. Burghoff, Y. Yang, J. L. Reno, and Q. Hu, "Dispersion dynamics of quantum cascade lasers," *Optica*, vol. 3, no. 12, pp. 1362–1365, 2016.